Cancer Nanotechnology

RESEARCH Open Access

Formulation and optimization of folate-bovine serum albumin-coated ethoniosomes of pterostilbene as a targeted drug delivery system for lung cancer: In vitro and in vivo demonstrations

Nemany A. N. Hanafy[1*], Reham H. Abdelbadea[2], Abdelaziz E. Abdelaziz[2] and Eman A. Mazyed[2]

*Correspondence:
Nemany.hanafy@nano.kfs.edu.eg

[1] Institute of Nanoscience & Nanotechnology, Kafrelsheikh University, 33516, Kafr ElSheikh, Egypt
[2] Department of Pharmaceutical Technology, Faculty of Pharmacy, Kaferelsheikh University, P.O.BOX 33516, Kaferelsheikh, Egypt

Abstract

This study aimed to overcome the poor solubility of pterostilbene (PTS) by developing promising reconstituted proethoniosomes (PENs). The reconstituted PENs loaded with PTS were fabricated according to a 2^3 factorial design by Design-Expert® software. The prepared ethoniosomes were assessed for entrapment efficiency (EE %) and % PTS released after 24 h (Q_{24h}). According to the desirability criteria, the ethoniosomal formula (F4) was chosen as the optimized formulation with EE% of 93.19 ± 0.66 and Q_{24h} of 75.10 ± 1.90%. The optimum ethoniosomal formulation was further coated with folic acid (FA) using bovine serum albumin (BSA) as a carrier and stabilizing agent and further evaluated for transmission electron microscopy (TEM), particle size, zeta potential, elasticity, Fourier transform infrared spectroscopy (FTIR), and stability. The targeted ethoniosomal formula appeared as spherical nanovesicles with a size of 144.05 ± 1.77 nm size and a zeta potential of -38.6 mV. The elasticity of the targeted ethoniosomal formula 19.27 ± 1.2 was higher than that of the corresponding niosome 1.48 ± 0.02. The targeted ethoniosomal formula showed high stability for three months. Fluorescence microscopy demonstrated an accumulation of FA-BSA-ethoniosomes in the cytoplasm of A549 cell lines. The observed therapeutic activity of the targeted ethoniosomal formula on lung cancer was explored by in vitro cytotoxicity on A549 lung cancer cells and in vivo animal models. The in vivo results were supported by histopathological analysis and immunohistochemical caspase-3 staining. FA-BSA-ethoniosomal formulation allowed specific targeting of cancer tissues overexpressing folate receptors. Overall, these results confirmed that the targeted ethoniosomal formula could be a promising nano-carrier for potential application as targeted cancer chemotherapy in clinical studies.

Keywords: Ethoniosome, Optimization, Targeting, Folate, Cancer

Graphical Abstract

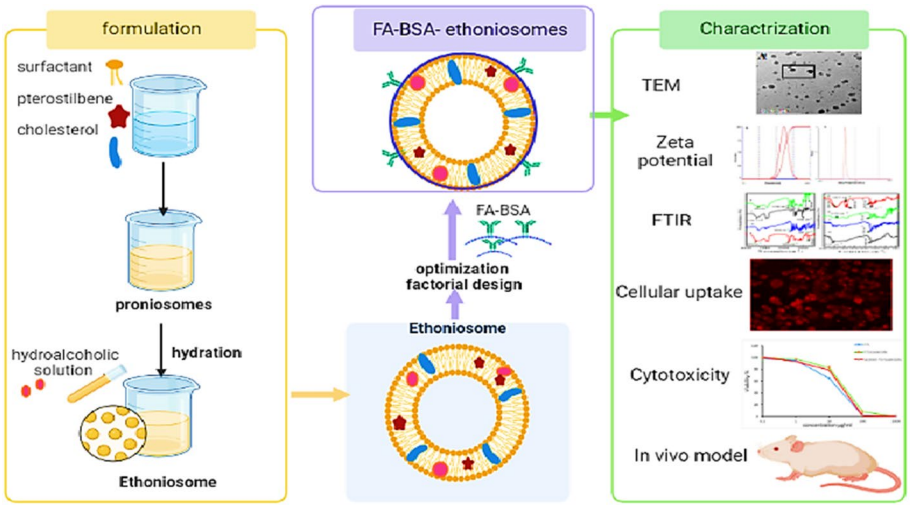

Introduction

Lung cancer is a common-leading cause of death in women and the first cancer killer in men. The incidence of lung cancer is approximately 4.9% in Egypt, accounting for about 7.3% of male cancers and 1.6% of female cancers. The high mortality rate makes lung cancer the fourth principal reason of death from cancer (Essa et al. 2022). The majority of patients were identified as having lung cancer after metastases. The fundamental cause of the low survival rate of patients having lung cancer is the variety of lung cancer stages and treatments. Nearly 50% of patients eventually die during the first year of diagnosis (Thakur and Overview 2019). Small cell lung carcinoma (SCLC) and non-SCLC (NSCLC) are the two primary types of lung cancer based on their histologic appearance, and they represent about 15% and 85% of all lung tumors, respectively (Zappa and Mousa 2016). Large cell carcinoma, squamous cell carcinoma, and adenocarcinoma are the three types of NSCLC (Inamura 2017). The primary treatment options for lung cancer are usually chemotherapy, radiation therapy, and surgery. However, multidrug resistance, recurrence, poor progression-free survival, severe toxicity, and overall survival are the limitations of each therapeutic regimen (Grossi et al. 2010).

Pterostilbene (PTS) is an example of a naturally occurring substance that can be utilized effectively in the management of cancer. PTS is a dimethylated derivative of resveratrol that is mostly found in blueberries, Pterocarpus marsupium, Pterocarpus santalinus, and grapes (Liu, et al. 2020) (Fig. 1). PTS has been discovered to exhibit several biological activities, including hypolipidemic, antioxidant, anti-diabetic, and anti-cancer properties. The anti-cancer activity includes the ability to inhibit the progression of gastric cancer cells, B16 melanoma cells, lung cancer cells, multidrug-resistant leukemia cells, and breast cancer cells (Lee et al. 2018; Chen, et al. 2018; Estrela et al. 2013). PTS has been reported to have antiproliferative and apoptotic

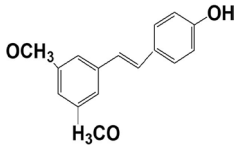

Fig. 1 Chemical structure of PTS

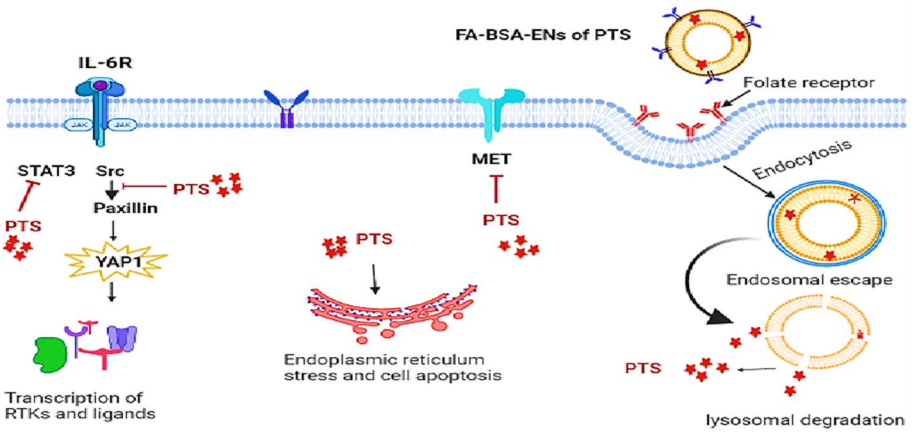

Fig. 2 The mechanism of PTS on lung cancer cell

effects on lung cancer. PTS blocks cellular kinase (Src), Paxillin, focal adhesion kinase (FAK), and signal transducer and activator of transcription-3 (STAT3) from activation. Additionally, PTS reduces the ability of triple-negative breast cancer (TNBC) cells to spread by primarily changing the Src-mediated signaling pathway. Furthermore, it has been discovered to lower the levels of mesenchymal markers, including Mesenchymal Epithelial Transition (MET). PTS also stresses the endoplasmic reticulum, which causes cells to undergo apoptosis (Fig. 2) (Bracht et al. 2019). PTS has a significant promise for use in pharmaceutical purposes. However, its uses and in vivo bioavailability are severely limited attributable to its poor water solubility and stability (Zhang et al. 2014).

It is well known that the active pharmaceutical ingredients and natural compounds with poor aqueous solubility and related limiting physicochemical qualities have been improved by using nanoparticle engineering procedures (Summerlin et al. 2015). The amphiphilic characteristic of conventional niosomes, surfactant-based nanovesicular systems makes them potential drug vehicles for hydrophilic and hydrophobic substances. In comparison to liposomes, they are also more physically and chemically stable (Rezaie Amale et al. 2021). Ethoniosomes (simply ENs) is a promising derivative of niosomes. ENs are an elastic type of conventional niosomes. Ethanol is a vital component in ENs as it improves the fluidity of the ethoniosomal membrane via intercalation into the vesicular lipid bilayer (Touitou et al. 2000). Therefore, drugs that are insoluble in ethanol cannot be formulated as ENs. The stability of ENs is higher than spanlastics due to their cholesterol content which minimizes agglomeration of ethoniosomal vesicles and drug leakage (Gaafar et al. 2014).

Niosomes also have several limitations, including aggregation, physical instability, hydrolysis, and leakage of the entrapped drug, which reduces the shelf life of the dispersion.

In previous studies, ENs were prepared by different methods such as the ethanol injection method (Mazyed et al. 2022) and the thin-film hydration method (Gaafar et al. 2014). For the first time, we have prepared ENs using the proethoniosomes (PENs) formulation method. Proethoniosomes (PENs) are a provesicular form that can be hydrated to produce ethoniosomes.

Proniosomes (PNs) are the provesicular type of niosomes and can be made as either a liquid crystalline gel or a free-flowing powder by coating a hydrophilic carrier with a non-ionic surfactant. PNs are reconstituted into niosomes upon hydration. Therefore, PNs could overcome the drawback of niosomes (Badria, et al. 2020a).

Meanwhile, the surface of a nanovesicle can be conjugated with several targeting ligands, such as Folic acid (FA), transferrin, and human epidermal growth factor receptor 2, to target tumor cells. For this reason, folic acid-conjugated bovine serum albumin (BSA) was used in the current study. BSA has been extensively used in biopharmaceutical applications because it offers several advantages, such as good biocompatibility, non-toxic, and excellent biodegradability. Additionally, BSA is employed as a carrier for targeting ligands, such as folate to enhance water solubility and stability (Li et al. 2015). Besides that, the structure of albumin amino acid content can target tumor cells by attaching with specific albumin-binding proteins, such as a secreted protein acidic and rich in cysteine and glycoprotein 60.

Indeed, folate receptors (FR) are overexpressed on many types of tumor cell surfaces. Therefore, during cellular uptake, FA-BSA-coated ethoniosomes can be derived and internalized into cancer cells via receptor-mediated endocytosis and release the drug into the prenuclear region of cancer cells (Chen et al. 2013; Sun et al. 2014).

The application of tumor-targeted delivery systems in the recent pharmaceutical industry aims to improve anti-cancer activity while reducing chemotherapy-related toxicity (Martín-Sabroso, et al. 2021). In our study, we prepared ethoniosomal nanovesicles of PTS coated with FA-conjugated BSA to improve the efficiency of PTS in the treatment of lung tumors.

Materials and methods

Materials

PTS was purchased from Xian Sgonek Biological Technology Co., Ltd. (China). Sorbitan monooleate (span 80) and sorbitan monostearate (span 60) were purchased from Oxford Lab Chemicals (Mumbai, India). Cholesterol (CHOL) was obtained from Advent Chembio Pvt. Ltd. (Mumbai, India). N-Nitrosodiethylamine (DENA) ISOPAC®, Folic acid (FA), albumin from bovine serum (BSA), dimethyl sulfoxide (DMSO), N-hydroxysuccinimide (NHS), and N-ethyl-N′-(3-dimethylamino propyl) carbodiimide hydrochloride (EDAC) were provided from Sigma Aldrich, St. Louis, MO, USA. Phenobarbital sodium (PB) was obtained from Alpha Chemika (Mumbai, India). Potassium dihydrogen phosphate and sodium hydroxide were provided by Alpha Chemical (Mumbai, India). Pharmaceutical-grade ethyl alcohol was purchased from El-Nasr Pharmaceutical Chemical Company (Cairo, Egypt). Nylon Acrodisc was provided by Gelman Sciences Inc., Ann

Arbor, MI, USA. Spectra/Pore® dialysis membranes (molecular weight cut-off 12,000–14,000 Dalton) were provided by Spectrum Laboratories Inc. (Rancho Dominguez, CA, USA). All other chemicals, solvents, and reagents were of analytical grade.

Methods

HPLC assay of PTS

The HPLC chromatographic study was achieved using a Thermo Scientific Dionex UltiMate HPLC system (Thermo ScientificTM, DionexTM, Sunnyvale, CA, USA. It is composed of a DAD-3000RS diode array detector, a WPS-3000RS autosampler, a TCC-3000RS column thermostat, and an LPG-3400RS quaternary pump. Chromeleon 7 software was used for the processing and collection of data. Various samples were injected into an RP-18 GP column (150 × 4.6 mm × 5 m), after being filtered using a nylon filter with a 0.45 µm pore size. The mobile phase used for PTS analysis was acetonitrile and double-distilled H_2O at a 65:35 volume ratio. The flow rate of PTS was adjusted at 1.0 mL/min and the injection volume was 20 µL (Tzeng et al. 2021). The detection wavelength of PTS was set at 309 nm and the retention time appeared at 4.9 min. The calibration curve included plotting peak areas of PTS versus the corresponding standard concentrations of ethanoic solutions of PTS ranging from 1 to 10 µg/mL. The current method was validated for the limit of detection (LOD), the limit of quantification (LOQ), accuracy, linearity, and interday and intraday precision.

Preliminary screening studies

Design optimal formulation The first step of the preliminary screening study was performed to identify the optimal condition that would be used for the preparation of PTS-loaded ENs using the ethanol injection method (EI) and the proniosome formulation method (PNs) via comparing the EE% of P1 and P2 (Table 1). The P1 and P2 formulations had the same composition but were prepared by different techniques; the ethanol injection and proniosome formulation methods, respectively.

The ethanol injection method (EI). The non-ionic surfactants, PTS (10 mg), and CHO were dissolved properly into absolute ethanol. The resulting ethanolic solution was carefully injected into an aqueous media that was preheated at 60 °C. The beaker was tightly enclosed to avoid ethanol evaporation. A milky ethoniosomal dispersion (10 mL) was formed after being continually stirred using a magnetic stirrer. After that, bath sonication was performed on the PTS-loaded ethoniosomal dispersions (water bath ultrasonicator, Elmasonic E 30 H, Elma, Schmidbauer GmbH, Singen, Germany). Then, to

Table 1 Choice of formulation technique of PTS-loaded ENs

Formula	Method of preparation	Span type	Amount of CHO %	Amount of ethanol %	*%EE
P1	PNs formulation	Span80	33	10	82.50 ± 1.75
P2	EI method	Span80	33	10	65.49 ± 1.35

EI, ethanol injection; PNs, proniosomes; EE, entrapment efficiency; CHO, cholesterol. Both formulations were prepared using 100 mg of span 80

* The values are described as mean ± SD ($n = 3$)

Table 2 The prescreening study for choosing the span type of PTS-loaded ENs

Formula	Span type	Amount of CHO %	Amount of ethanol %	* %EE
P3	Span80	33	20	80.35 ± 1.9
P4	Span60	33	20	93.8 ± 0.90

EE, entrapment efficiency; CHO, cholesterol. Both formulations were prepared using 100 mg of span 60 and span 80 by PNs formulation method

* The values are described as mean ± SD (n = 3)

Table 3 The prescreening study for the choice of components of PTS-loaded ENs

Formula	Span type	Amount of CHO %	Amount of ethanol %	*%EE
P5	Span60	33	10	94.77 ± 3.25
P6		33	30	84.66 ± 0.43
P7		50	30	90.0 ± 1.76
P8		66	30	81.77 ± 3.25

EE, entrapment efficiency; CHO, cholesterol. All formulations were prepared using 100 mg of span 60 by the PNs formulation method

* The values are described as mean ± SD (*n* = 3)

allow them for full maturity, the ethoniosomal formulations were kept at 4 °C overnight (Mazyed et al. 2022).

The proniosome formulation method (PNs). The accurate weight of the non-ionic surfactants, CHO, and PTS (10 mg) were dissolved using 200 µL ethanol. The resulting mixture was heated for 5 min at 65 ± 1 °C in a sealed vessel to produce a clear liquid system. The addition of a volume of the aqueous phase equivalent to that of ethanol was achieved while the mixture was heated until it became clear. This mixture was left to cool at room temperature with continuous mixing until it was converted to proethoniosome gel. The proethoniosome gel was wetted with 10 mL of the hydroalcoholic solution by mechanical stirring for 30 min until the milky ethoniosomal dispersion was formed. The resulting ethoniosomal dispersions were sonicated in a bath sonicator for 30 min (Gaafar et al. 2014; Maghraby et al. 2015).

Choice of components of PTS-loaded ENs The second step of the preliminary screening test was operated to choose the proper constituents of PTS-loaded ENs such as type of span (span 60 or span 80) (Table 2), amount of used ethanol, and amount of used CHO (Table 3).

The prepared PTS-loaded ENs were evaluated according to their entrapment efficiency (EE%) which would demonstrate the vesicular integrity of ENs and confirm the absence of PTS leakage out the surface of ENs.

Preparation of PTS-loaded ethoniosomal formulations

The PTS-loaded ENs were prepared by the proniosome formulation method (as described above). Optimization of PTS-loaded ENs was achieved by a 2^3 factorial design to evaluate the effect of the independent variables on different responses. The three factors were checked twice: first at the lower level (-1) and again at the upper level (+ 1). The amount of span 60 (X1), amount of ethanol (X2), and amount of CHO

(X3) were the independent variables. The experimental trials were carried out using eight preparations of PTS-loaded ENs using Design-Expert software, Version 7.0.0 (Stat-Ease, Inc., Minneapolis, MN, USA). The entrapment efficiency (EE%, Y1) and the percentage of drug released after 24 h were dependent variables (Q_{24h}, Y2) (Peram et al. 2019). To demonstrate the quality of fit of the present model to the experimental results, the coefficient of determination (R^2), predicted ^{2}, and modified R^2 were calculated. The data were statistically investigated using analysis of variance (ANOVA) to determine the significance level of variables using the p-value and F-statistics (Pathan et al. 2018).

Determination of entrapment efficiency of PTS-loaded ENs EE% of PTS-loaded ENs was determined by using the dialysis technique (Eid et al. 2019; Maestrelli et al. 2005) via separation of free PTS. PTS-loaded ENs (10 mL) were incubated for 12 h at 25 ± 0.5 °C in a dialysis bag against 100 mL distilled water. The amount of the free un-entrapped PTS found in the dialysate was measured using HPLC at 309 nm (Tzeng et al. 2021).

The following equation was used to determine EE%:

$$EE\% = (C_{ENs} - C_{PTS})/C_{ENs} * 100, \quad (1)$$

where C_{ENs} is the total concentration of the PTS in ENs and C_{PTS} is the free un-entrapped PTS concentration.

In vitro release study of PTS-loaded ENs The solubility of PTS was determined in 100 mL distilled water and the dissolution medium using a saturation flask-shaking technique (Larsson 2009) (Additional file 1: Data).

The in vitro drug release of entrapped PTS from ENs was studied using the dialysis bag diffusion technique (Maghraby et al. 2014). The dialysis tubing was soaked overnight in distilled water to confirm the complete swelling of the dialysis membrane before cutting it into suitable pieces. PTS-loaded ENs (2 mL), or an equivalent amount of PTS, were inserted into the tightly sealed cellophane membrane dialysis bag. The dialysis bag was further immersed in 200 mL of a phosphate-buffered saline solution (PH = 7.4). Ethanol was added to the media to assure the achievement of sink condition. The entire system was set at 37 ± 0.5 °C with 400 rpm/min continuous magnetic stirring. Glass beakers were sealed with Parafilm® to prevent alcoholic vaporization. To resave a consistent volume of the receptor medium, 1 mL aliquots were removed at predefined intervals and replaced with an equivalent volume of fresh media. The collected samples were diluted and examined using HPLC at 309 nm after filtering through a 0.45 µm nylon membrane filter (Salem, et al. 2021).

The experiments were repeated three times. The results were then described as mean with standard deviations. A kinetic analysis using several mathematical models was used to study the mechanism of the in vitro PTS release from the reconstituted PENs (Mazyed and Abdelaziz 2020).

Statistical optimization of PTS-loaded ENs The acceptability values explain how near the selected responses are to their optimum values. They were utilized to determine

the optimized formula. The formulation that had the highest desirability value was selected as the optimized formula. The optimal formula for the current investigation was chosen based on the highest EE% and the highest Q_{24h} (Badria, et al. 2020b).

Preparation of FA-BSA-ENs of PTS

The carboxylic group of FA was activated by adding 20 mg FA into 2 mL DMSO and stirring continuously until dissolved completely. NHS (10 mg) and EDAC (30 mg) were mixed with the FA solution and agitated for 30 min. Conjugation of FA to bovine serum albumin (BSA) was performed by adding 1 mL activated FA solution to the BSA solution (50 mg/100 mL) and then agitating for 30 min. The optimized ethoniosomal formula (10 mL) was functionalized by adding 20 mL of conjugated BSA-FA with a magnetic stirrer for 20 min to prepare FA-BSA-ENs (Hanafy et al. 2017; Mabrouk Zayed et al. 2022).

Characterization of FA-BSA-ENs of PTS

Transmission electron microscopy (TEM) The morphological structure of the optimized FA-BSA-ENs was determined by transmission electron microscopy (JEOL 2100, Tokyo, Japan). An amount of 1 mL of freshly manufactured FA-BSA-ENs was diluted appropriately with deionized water and carefully dropped onto a carbon-coated grid and drained off the excess. The sample was left for 5 min to dry and then observed under TEM (Bansal et al. 2013).

Determination of particle size and zeta potential The particle size and zeta potential of FA-BSA-ENs of PTS were measured by Zetasizer (NICOMP 380 ZLS Zeta Potential/Particle Sizer, Santa Barbara, CA, USA). The method is based on the light scattering technique. The FA-BSA-ethoniosomal formula was diluted with deionized water (Sezgin-Bayindir et al. 2013).

Elasticity measurement The elasticity of the FA-BSA-ENs and its corresponding niosomal formula (the niosomal formula had the same composition as the optimized ethoniosomal formula without adding ethanol) was measured by the extrusion method. The ethoniosomal and niosomal formulas were extruded by using a filter membrane with a pore size of 200 nm and 2.5 bar of pressure. The amount of vesicular suspension extruded over 5 min was determined for each formula (Mehanna et al. 2015).

$$E = \mathrm{J}\,(vs/ps)^2, \tag{2}$$

where E is the elasticity of the vesicle, J is the amount of extruded dispersions, v_s the vesicle size of the extruded formulas, and p_s is the pore size of the membrane filter.

Fourier transform infrared spectroscopy (FTIR) PTS, span 60, CHO, PTS-loaded ENs, BSA, FA, and FA-BSA-ENs of PTS samples were investigated by infrared spectroscopy measurement. The infrared spectroscopic analysis was determined using the FTIR spectrometer in the transmittance mode (FTIR Shimadzu 8300 Japan). In a hydraulic press, the samples were combined separately with potassium bromide and compacted

to produce KBr pellets (Kimaya Engineers, Maharashtra, India). In the range of 4000–400 cm^{-1}, all spectroscopic bands were obtained with a resolution of 4 cm^{-1}(Arzani et al. 2015).

The stability study

The stability of the FA-BSA-ENs of PTS and the PTS-loaded ENs was investigated according to their EE% and Q_{24h}. For the stability experiment, the ethoniosomal dispersions were maintained at (4 ± 2 °C) for 90 days in sealed glass containers according to ICH stability guidelines (Mazyed et al. 2022).

Cellular uptake and targeting capacity

A549 cells (10^6) were grown upon the surface of a sterilized coverslip that was inserted into the bottom of 6-multiwell plates. After 24 h of growth, 30 µg/mL of Rhodamine-FA-BSA-ENs and Rhodamine-PTS-loaded ENs were added to each well and then incubated for 24 h in a humidified 37 °C and 5% CO_2 environment. Phosphate buffer saline was used to clean the A549 cell lines before they were fixed with 4% paraformaldehyde. Cellular uptake was examined after 24 h using red (TRITC) channel of fluorescence microscopy, and then images were captured using a digital camera. The intensity of collected ENs in the perinuclear region of the cytoplasm was used to determine targeting capacity. The corrected total cell fluorescence (CTCF) was calculated according to Hanafy et al. (2023) by using this formula

$$\text{CTCF} = \left(\text{mean fluorescence of background readings} \times \text{area of a selected cell}\right) - \text{integrated density.}$$

In vitro cytotoxicity study on A549 cell lines

Cell viability of FA-BSA-ENs of PTS, PTS-loaded ENs, and free PTS was performed using sulforhodamine B (SRB) assay against lung cancer (A549) cell lines. Cells were seeded in 96-well microplates at a density of 5×10^3 cells/well. After their overnight incubation, cells were then treated with FA-BSA-ENs of PTS, PTS-loaded ENs, and free PTS at serial concentrations (0.01, 1, 10,100, and 1000 µg/mL) for 72 h. The serial concentration was used according to the equivalent concentration of PTS. After cell treatment, trichloroacetic acid (TCA) reagent was added and cells were incubated at 4 °C for 1 h. After that, the cells were washed carefully with PBS pH 7.2 and then SRB solution was added and incubated in a dark place at 37 °C for 10 min. Moreover, the dissolution of protein-bound SRB stain was performed by adding TRIS. The absorbance was measured at 540 nm using a BMG LABTECH®-FLUOstar Omega microplate reader (Ortenberg, Germany). The IC50 value was recorded as the concentration that exhibited 50% of cell viability (Allam et al. 2018; Skehan et al. 1990).

In vivo study

This experiment was managed according to the standard protocol established by the Committee of Ethics, Faculty of Pharmacy, Kafrelsheikh University, Egypt (Approval

number KFS-ph-00121/). The "Egyptian Organization for Biological Products and Vaccines" provided 80 healthy adult male Wistar mice weighing 22 ± 4 g (Agouza, Giza, Egypt). During the experiment, they were kept in a well-ventilated environment with a 12-h light–dark cycle, a humidity of 55%, and a temperature of 21–25 °C. The mice were given a consistent diet and free access to water (ad libitum) (Abdel-Hamid et al. 2018).

Mice were adapted for one week before being randomized to one of two groups: the control group ($n = 40$) was given a single dose of saline intraperitoneally, while the lung cancer group ($n = 40$) was given a single dose of DENA (200 mg/kg) intraperitoneally. After 14 days, only the lung cancer group received 0.05% phenobarbital sodium in their drinking water for the next 18 weeks.

To monitor the tumor induction, the histopathology investigation was done continuously by using H + E until revealing the presence of lung cancer nodules (Sivalingam et al. 2019). Meanwhile, the body weight was determined weekly for all of the experiments.

The mice were divided into the following groups:

Group (I): Mice with lung cancer treated with targeted FA-BSA-ENs of PTS, (100 mg/kg) orally for two weeks.

Group (II): Mice with lung cancer treated with non-targeted PTS-loaded ENs, (100 mg/kg) orally for two weeks.

Group (III): Mice with lung cancer treated with PTS, (100 mg/kg) orally for two weeks.

Group (IV): Mice with lung cancer without treatment.

Group (V): Healthy normal mice treated with targeted FA-BSA-ENs of PTS (100 mg/kg) orally for two weeks.

Group (VI): Healthy normal mice treated with non-targeted PTS-loaded ENs, (100 mg/kg) orally for two weeks.

Group (VII): Healthy normal mice treated with PTS, (100 mg/kg) orally for two weeks.

Group (VIII): Healthy normal mice without treatment.

The mice were sacrificed by neck amputation at the end of the 20th week, and tissue samples from the lungs, liver, heart, and kidney were removed for histopathological staining and immunohistochemistry analysis for caspase-3.

The in vivo anti-tumor efficacy

The efficacy of the anti-tumor drug was evaluated by using histopathology and immunohistochemistry to confirm the inhibition of tumor growth and to investigate the preventive cancer cell spreading from the primary tumor.

Histopathological analysis Specimens of the lung, liver, kidney, and heart were fixed in a 10% buffered formalin solution (pH 7.4). The specimens were further dehydrated in a series of ethanol dilutions. After that, the specimens were immersed in paraffin wax for 24 h at a temperature of 56 °C. The created paraffin wax blocks were sliced into 5 µm thick parts. Sections of the lung, liver, kidney, and heart were stained with hematoxylin and eosin (H&E) and then visualized using a light microscope. A digital camera linked to a computer system was used to capture photographs of morphologi-

cal changes (Nikon digital camera, Japan) (Hanafy et al. 2021). After that, the photographs were analyzed by Image J software (https://imagej.en.softonic.com/download).

Immunohistochemistry analysis Immunohistochemistry was used to detect caspase-3 in lung Sects. (5 μm thick). The sections were deparaffinized and rehydrated. Antigen retrieval was carried out in a pH 6.0 citrate buffer. In addition to blocking endogenous peroxidase by using 3% hydrogen peroxide, 1% BSA was also used to block non-specific binding sites.

After that, sections were treated with an anti-mouse caspase-3 monoclonal antibody (Abcam Inc., 1:200 dilution) and an anti-rabbit antibody conjugated with horseradish peroxidase. As a chromogen, a solution of 3,3'-diaminobenzidine (2%) was utilized. The slides were counterstained with H&E. The staining intensity was then calculated and reported as a % of positive cells/1000 lung cancer cells (Abdel-Hamid et al. 2022).

Statistical analysis

SPSS-11 software was used to statistically evaluate the data (SPSS Inc., Chicago, IL, USA). The statistical analysis was performed by Student's t-test and analysis of variance (ANOVA). All data obtained from repeated measurements were expressed as the mean SD. The P-value was considered significant when $P < 0.05$.

Results and discussion

HPLC assay of PTS

A validated HPLC technique was operated to detect the concentrations of PTS in PTS-loaded ENs (Fig. 3). Peaks of PTS were observed at 309 nm (Tzeng et al. 2021). The PTS calibration curve was plotted, and the R^2 value showed a good value (0.995). PTS chromatograms revealed no presence of interfering peaks. This could demonstrate that the other ingredients in the ethoniosomal formulations did not affect the estimation of PTS. The PTS retention time appeared at 4.9 min. This method was more confident as

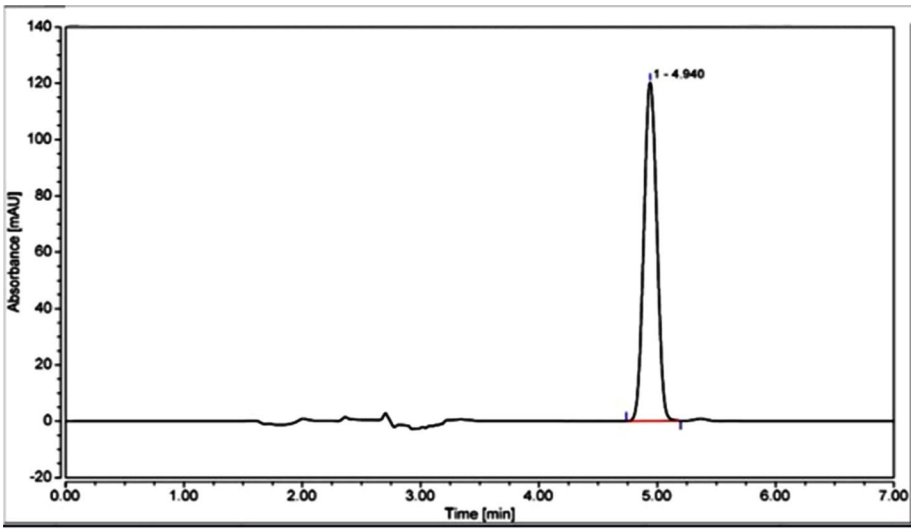

Fig. 3 HPLC chromatogram of PTS

a precise and simple methodology for PTS analysis. Additionally, it was considered an economic method due to its low retention time which decreased the run time and solvent consumption during analysis. The percentage recovery, which varied from 98–102 to 97–102% for inter- and intraday, respectively, shows that the obtained data were accurate. Meanwhile, the relative standard deviation (RSD) values, which were in the acceptable range, demonstrated the accuracy of the method. The LOD and LOQ values, which were 0.2 µg/mL and 0.5 µg/mL, respectively, demonstrated the sensitivity of the technique.

Preliminary screening study

Choice of formulation technique

The outcome data explored that the PNs formulation method (P1) was superior compared to the EI method (P2) on EE% ($p < 0.05$) (Table 1). The PNs formulation method showed better surfactant/lipid hydration when compared to the EI method. This might be attributable to inadequate solubility of the surfactant in absolute ethanol that could negatively affect the availability of surfactant/lipid for the fabrication of ENs. This result is in agreement with Gaafar et al. (Gaafar et al. 2014).

Choice of component of PTS-loaded ENs

According to the type of span, the EE% of the ethoniosomal formula prepared using span 60 (P4) > the EE% of these prepared using span 80 (P3) (Table 2). The head groups in span 80 and span 60 are identical but the alkyl chain of span 80 is unsaturated. Therefore, the permeability is markedly increased upon the addition of that double bonds to paraffin chains, which may help understand the reduction in EE% of formulations contained span 80. In addition, the transition temperature of span 80(_12 °C) is lower than that of span 60(53 °C) (Mokhtar et al. 2008).

It was observed that ENs containing the highest ethanol level (P6) had the lowest EE% ($p < 0.05$) compared with (P5) which contains a lower ethanol level (Table 3). That might be attributable to increasing the fluidization of the ethoniosomal membrane resulted in enhancing drug leakage out from PTS-loaded ENs. These outcomes agreed with Ahad et al. (Ahad et al. 2013) who demonstrated that the EE% increased significantly with increasing ethanol concentration from 20 to 35%.

Concerning the CHO concentration, PTS-loaded ENs containing 66% CHO (P8) had the lowest EE% in comparison to those (P6 and P7) having 33% and 50%, respectively (Table 3). The results showed a potential increase in EE % with increasing CHO concentration up to 50%, while a significant reduction in EE% was obtained with increasing CHO above 50% (P8). The result confirmed that increasing the concentration of CHO led to an increase in the bilayer lipophilicity and stability resulting in decreasing the permeability. For this reason, the EE% of the lipophilic drug into bilayers was improved (Bernsdorff et al. 1997; Kirby et al. 1980). On the other hand, if the concentration of CHO became higher than 50%, this may struggle with the drug for the packing area within the bilayer, preventing the drug from assembling into vesicles (Maghraby et al. 2004). Another study hypothesized that the normal linear shape of vesicular membranes

Table 4 Composition of PTS-loaded EN according to 2^3 Factorial design

Formula	Variables				
	Independent Variables			Dependent Variables	
	X1	X2	X3	Y1*	Y2*
F1	− 1	1	1	94.61 ± 0.90	71.22 ± 0.25
F2	− 1	1	− 1	91.00 ± 0.63	85.83 ± 0.55
F3	1	1	1	95.31 ± 3.94	74.70 ± 0.71
F4#	1	1	− 1	93.80 ± 0.90	74.85 ± 1.15
F5	− 1	− 1	1	95.96 ± 3.61	52.71 ± 0.61
F6	− 1	− 1	− 1	92.81 ± 1.80	71.38 ± 0.49
F7	1	− 1	1	96.60 ± 2.39	63.06 ± 0.36
F8	1	− 1	− 1	94.77 ± 3.25	67.5 ± 0.353
Independent variables		Low (− 1)		High (+ 1)	
X1: Amount of span 60 X2: Amount of ethanol X3: Amount of CHO		25 mg 10% 25 mg		100 mg 20% 50 mg	

Q_{24h}, percentage of PTS released after 24 h; EE, entrapment efficiency

optimized Formula, * the data are expressed as mean ± SD ($n = 3$); all formulations included 10 mg PTS, Y1: EE (%), Y2: Q_{24h} (%)

Table 5 Obtained data of the 2^3 factorial design of PTS-loaded ENs

Response	R^2	Adjusted R^2	Predicted R^2	Adequate Precision
EE% (Y1)	0.9266	0.8715	0.7062	11.830
Q_{24h} (Y2)	0.9999	0.9998	0.9992	390.001

R^2, coefficient of determination; EE, entrapment efficiency of PTS-loaded ENs; Q_{24h}, % PTS released after 24 h

may be disrupted by an increase in CHO above a specific concentration, which would result in a decrease in entrapment efficiency (El-Samaligy et al. 2006). These results are in agreement with Mavaddati et al. (Mavaddati et al. 2015) who found that the EE% of dexamethasone in the span 60 niosomes significantly increased with increasing cholesterol level from 25 to 50%, followed by a decrease in EE% upon a further increase in cholesterol level above 50%.

Regarding the preliminary screening study, the PNs formulation method was chosen for the preparation of PTS-loaded ENs using span 60, 50% CHO, and 10% *v*/*v* ethanol.

Analysis of the factorial design

To evaluate the data and to improve PTS-loaded ENs formulation, a three-factor, two-level (2^3) model was used with the Design-Expert software, Version 7.0.0 (Stat-Ease, Inc., Minneapolis, MN, USA). Three different variables, including the amount of span 60 (X1), amount of ethanol (X2), and amount of CHO (X3), were evaluated, whereas the two dependent variables were EE% (Y1) and % Q_{24h} (Y2). The selected factors with their two levels and the dependent variables are recorded in Table 4. The positive sign in front of the independent variable revealed that the factor had a synergistic effect on the measured responses. Nevertheless, the negative sign exhibited an antagonistic impact (Araújo

et al. 2010). The optimized PTS-loaded ethoniosomal formula was selected depending on maximum values of EE% (Y1) and Q_{24h} (Y2).

This model demonstrated that the R^2 for EE% (Y1) and Q_{24h} (Y2) obtained relatively high values (0.9266 and 0.9999, respectively) showing that the outcome data were statistically significant (Table 5). The predicted R^2 and adjusted R^2 were computed to estimate the well fit of the regression model with the experimental data (Turk et al. 2014). The values of predicted R^2 and adjusted R^2 for different responses should be within around 0.20 of each other to be in reasonable agreement. Moreover, adequate precision determined the signal-to-noise ratio which confirms the availability of operating the design space navigation. The value of adequate precision which was more than 4 (11.83 and 390.00) for EE% and $Q_{24h,}$ respectively, is considered acceptable (Table 5)(Badria, et al. 2020b).

The obtained data were calculated using the (ANOVA) analysis (Table 6). Thus, the significance of the experimental results to various models is shown by a p-value ($P < 0.05$), which results in the refusal null hypothesis (H_0) for the alternative hypothesis. This is in agreement with Badria et al. (Badria, et al. 2020a).

Additionally, diagnostic graphs of both EE % and Q_{24h} were employed to analyze the accuracy and validity of this model. The expected and experimental values of various responses (EE % and Q_{24h}, respectively) show a strong correlation (Additional file 1: Figures S1 and S2). The residuals were described as the variation between the expected and actual values of the two responses.

The residuals were described as the variation between the expected and actual values of the two responses. The normal probability of residuals is shown in Additional file 1: Figures S1a and S2a as linear patterns that were normally distributed. There was no deviation observed and all dots lie tightly near a straight line. Therefore, the model efficiently improved the correlation between the variable and responses.

Additional file 1: Figure S1b and S2b indicates that the colored marks, which represented the two measured responses, were randomized surrounding the zero axis and confirmed the absence of constant error. Additional file 1: Figure S1c and S2c shows residual versus run plots with a uniform and random distribution of values, demonstrating the lake of lurking variables. In the current model, predicted and actual values of

Table 6 ANOVA for the 2^3 factorial design of PTS-loaded ENs

Response	Source	Sum of Squares	df	Mean Square	F-Value	*P*-value
EE% (Y1)	Model	21.03	3	7.01	16.82	0.0099
	X1	4.68	1	4.68	11.24	0.0285
	X2	3.65	1	3.65	8.75	0.0417
	X3	12.70	1	12.70	30.48	0.0053
Q_{24h} (Y2)	Model	650.86	6	108.48	13,193.90	0.0067
	X1	24.62	1	24.62	2994.45	0.0116
	X2	337.15	1	337.15	41,006.66	0.0031
	X3	6.65	1	6.65	809.09	0.0224

Values of $p < 0.05$ indicate that the model is significant, X1: the amount of span 60, X2: the amount of ethanol, X3: the amount of CHO

EE, entrapment efficiency; Q_{24h}, % PTS released after 24 h; df, degree of freedom

EE% and Q_{24h} were normally distributed and were near a straight line (Additional file 1: Figures S1d and S2d).

The effect of independent variables on EE% of PTS-loaded ENs.

EE% of PTS-loaded ENs ranged from 91 ± 0.63 to 96.6 ± 2.39 (Table 4). As a result, PTS was successfully incorporated into the ethoniosomal formulations, proving the effectiveness of utilizing ENs as a lipophilic drug delivery system. Moreover, the independent parameters (amount of span 60, amount of ethanol, and amount of CHO) exhibited a significant impact on EE % of the PTS-loaded ENs as shown in Additional file 1: Figure S3 and Table 6.

Table 6 provides illustrations of the EE% according to ANOVA findings. The level of span 60 (X1) and CHO (X3) had a positive influence on the EE %, whereas ethanol(X2) had a negative impact ($p < 0.05$). This might be explained on the basis of the distribution of CHO within the bilayer would increase the lipophilicity of the bilayer and decrease its permeability. So, it stabilized the membrane, which in turn caused an elevation in the EE % of ENs. This effectively trapped the lipophilic drug in the vesicular bilayer of the ENs (Moghassemi and Hadjizadeh 2014). These results agreed with El-nesr et al. (Ola et al. 2010) who reported that the entrapment efficiency of fluconazole increased by increasing the CHO content.

Additionally, in the case of increasing span 60, the EE % of ENs also increased which may be explained by the presence of more ethoniosomal vesicles and good ethoniosomal cores (Shah et al. 2019). These results are consistent with Srinivas et al. (Srinivas et al. 2010) who found that the entrapment efficiency of niosomes containing aceclofenac increased when the concentration of surfactant (span60 or span 20) increased.

On the other hand, increasing the concentration of ethanol led to a decrease in the EE%. This could be attributed to the gradual solvation of the bilayer membrane caused by the higher concentration of ethanol (Ahad et al. 2013).

The effect of independent variables on Q_{24h} of PTS-loaded ENs

The solubility of PTS in distilled water and the dissolution medium was found to be 0.8 ± 0.13 µg/mL and 82.59 ± 1.5 µg/mL, respectively (Additional file 1: Data).

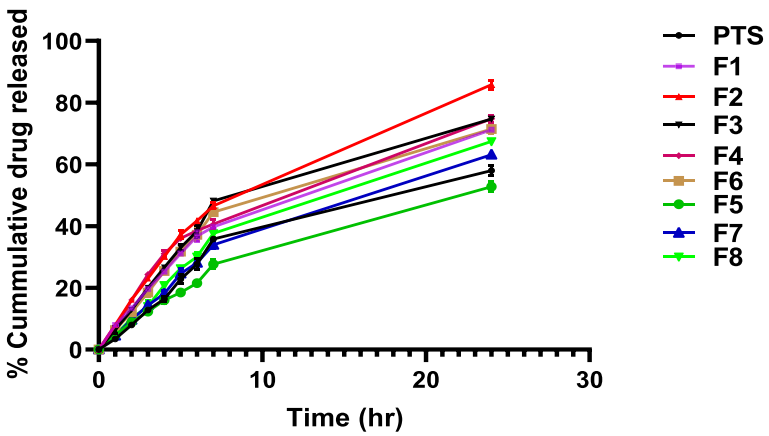

Fig. 4 The in vitro release profile of PTS-loaded ENs and PTS dispersion for 24 h

All formulations were used to calculate the in vitro release of PTS from PTS-loaded ENs. All PTS-loaded ENs showed a higher release rate of PTS than pure PTS. The PTS % released from PTS-loaded ENs after 24 h ranged from 53 to 86%, while 57% was released from pure PTS within the same time as shown in (Fig. 4) (Salem, et al. 2021).

The substantial effects of several independent factors on Q_{24h} of PTS-loaded ENs are shown in Additional file 1: Figure S4 and Table 4. There was a significant negative impact of the amount of span 60 (X1) on Q_{24h} of PTS-loaded ENs ($p < 0.05$). This could be attributed to the formation of vesicular bilayers with stiffness properties that prevented drug leakage out of ethoniosomal vesicles (Mazyed et al. 2022). These results are in accordance with Anbarasan et al. who (Anbarasan et al. 2013) reported that the amount of capecitabine released from niosomes decreased with an increase in the surfactant concentration.

The amount of ethanol(X2) had a substantial favorable impact ($p < 0.05$) on the Q_{24h} of PTS-loaded ENs. It assumed that the smoothness and flexibility that ethanol provided on the vesicles facilitated the diffusion of PTS via the vesicle membrane (Salem et al. 2020).

The amount of CHO(X3) had a significant negative impact on Q_{24h} of PTS-loaded ENs ($p < 0.05$). This result may be due to the stiffness of the bilayer which played a major role in the in vitro release of PTS from ENs. In this case, when the CHO level increased, the PTS efflux decreased because CHO caused the potential stabilizing membranes. Owing to its ability to block vesicular bilayer spaces, which reduced drug release (Nasr 2010). Mansouri et al. (Mansouri et al. 2021) found that when the amount of cholesterol in the streptomycin sulfate-loaded niosomes increased, the amount of streptomycin sulfate released from the vesicles decreased.

Table 7 shows the kinetic analysis of all PTS-loaded ENs and PTS suspension in terms of (R^2) values that were discovered by linear regression models. The findings demonstrated that the Higuchi model represented the kinetic release of all PTS-loaded EN. This is in agreement with Mazyed et al. (Mazyed and Abdelaziz 2020). The Higuchi model described that PTS diffused from ethoniosomal vesicles based on the Fickian diffusion Equation except for PTS dispersion, F3, and F6 which obeyed first-release order kinetics.

Table 7 Kinetics analysis after the in vitro release of PTS-loaded ENs according to the correlation coefficient values

Formula	Zero Order	First Order	Higuchi Model	Hixson Crowell	Baker-Lonsdale
F1	0.9505	− 0.9839	0.9920	− 0.354811219	− 0.159839084
F2	0.9552	− 0.9881	0.9947	− 0.34372876	− 0.160173991
F3	0.9224	− 0.9884	0.9773	− 0.285463503	− 0.109092517
F4	0.9400	− 0.9847	0.9890	− 0.385148849	− 0.212569072
F5	0.9737	− 0.9756	0.9961	− 0.349325635	− 0.138807883
F6	0.9266	− 0.9868	0.9800	− 0.292703242	− 0.116659442
F7	0.9607	− 0.9804	0.9941	− 0.301207217	− 0.119702986
F8	0.9544	− 0.9826	0.9911	− 0.284109604	− 0.108479532
PTS	0.9327	− 0.9816	0.9792	− 0.245530879	− 0.080418386

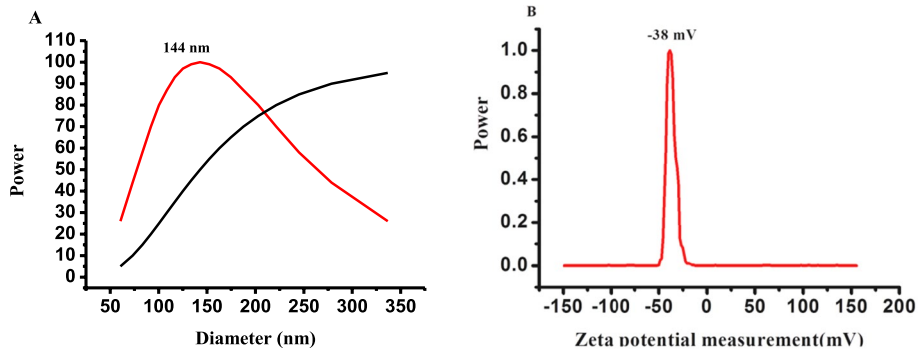

Fig. 5 **A** Lognormal size distribution **B** zeta potential of FA-BSA-ENs of PTS

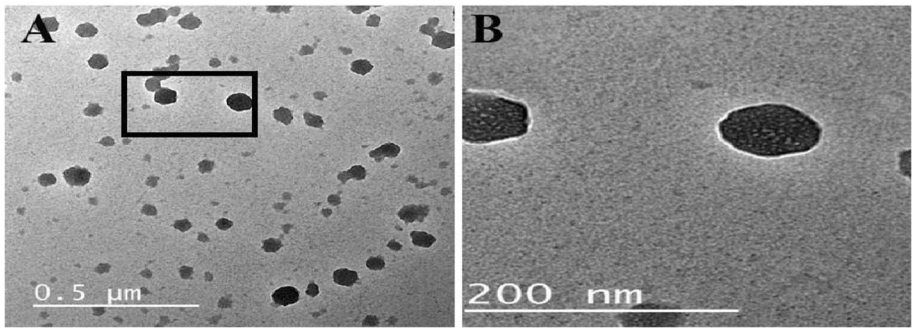

Fig. 6 TEM image of FA-BSA-ENs of PTS

Optimization of PTS-loaded ENs

The optimizing PTS-loaded ethoniosomal formula was obtained by the point prediction model of the Design-Expert software® based on the parameters of maximizing Q_{24h} and EE %. The findings showed that F4 fulfilled the criteria of an optimum formula. The value of EE% and Q_{24h} of the optimizing formula was 93.8% and 74.8%, respectively. Thus, F4 could be considered the optimal ethoniosomal formula.

Characterization of the optimized FA-BSA-ENs of PTS

Determination of particle size and zeta potential

The FA-BSA-ethoniosomal formula was evaluated according to particle size, polydispersity index (PDI), and zeta potential. Our findings showed that the size of the FA-BSA-ENs was 144.05 ± 1.77 nm.

PDI is a measurement of the homogeneous size distribution of the ethoniosomal vesicle. Since the degree of homogeneity obtained between the individual particles increased when the PDI value approached zero. The value of PDI for FA-BSA-ENs was 0.333 (PDI < 0.5), representing a narrow and symmetric size distribution (Fig. 5A).

The stability of the ethoniosomal formulation was determined by a high value of zeta potential (positive or negative charges). The zeta potential of FA-BSA-ENs of PTS was − 38.6 mV, showing that the FA-BSA-ethoniosomal vesicle was highly stable. The highly stable and uniform dispersion may be the result of a repulsive force between ethoniosomal vesicles that inhibited their aggregation (Fig. 5B).

Transmission electron microscopy (TEM)

The morphological characterization of the optimized FA-BSA-ethoniosomal formula was investigated by TEM. TEM showed semispherical vesicles which were uniformly distributed throughout the formulation (Fig. 6). Their assembly indicated that the ethoniosomal vesicle was successfully formed.

Elasticity measurement

The flexibility of the ethoniosomal vesicles refers to their capacity to cross the minuscule pores of cellular membranes without disturbing vesicular integrity. The elasticity of the FA-BSA-ENs of PTS (19.27 ± 1.2) was significantly higher than the corresponding niosomes (1.48 ± 0.02) ($p < 0.05$).

The size of vesicle of the ethoniosomal vesicles and the niosomal formulations was estimated before and after extrusion (Table 8). The results indicated that the FA-BSA-ENs of PTS showed no significant difference ($P > 0.05$) in the size of the vesicle before and after extrusion. This may be attributed to the presence of ethanol in the fabrication of PTS-loaded ENs that could interact with the polar head region of the surfactant molecules, resulting in increasing the fluidity of the bilayer membranes. However, the vesicle size of PTS-loaded niosomes was significantly decreased ($p < 0.05$) after extrusion. It could be explained by the lack of deformability of the niosomal vesicles which caused the rupture of the vesicle during passage through the nylon membrane (Mazyed, et al. 2021). The high elasticity of the ENs could reduce the risk of vesicle rupture while allowing them to penetrate biological membranes without any cellular deformability. These results agreed with Leonyza et al. (Leonyza and Surini 2019) who reported that the vesicles with high membrane deformability could penetrate the lipid membrane without losing their vesicle integrity. Additionally, Mazyed et al. (Mazyed et al. 2022) reported that the elasticity of transethoniosomes was significantly higher than that of the corresponding niosomes.

Fourier transform infrared spectroscopy (FTIR)

In the current study, the structure of assembly was studied by using FTIR using the component of structure as follows: pure PTS, pure CHO, pure surfactant (span 60), PTS-loaded ENs (F4), FA-BSA-ENs of PTS, BSA, and FA (Fig. 7). Since the PTS spectrum showed a characteristics peak related to the O–H group at 3493 cm^{-1}, several absorption bands were found in the range of 750–1600 cm^{-1}, including 1608, 1586.1, 1514.1, and 1456.3 cm^{-1} associated to the benzene aromatic ring (Liu et al. 2021).

The spectrum of span 60 showed a band located at 1743 cm^{-1} corresponding to the C = O stretching vibration. The band at 1171 cm^{-1} was attributed to –C–CO–O–.

Table 8 Determination of the elasticity of FA-BSA-ENs and the corresponding niosomes

Formula	PS before extrusion (nm)	PS after extrusion (nm)	E
FA-BSA-ENs	144.05 ± 1.77	142.8 ± 1.20	19.27 ± 1.2
Niosomes	314.30 ± 1.78	109 ± 1.68	1.48 ± 0.02

Each value represents mean ± SD ($n = 3$),

PS, particle size; E, elasticity; FA, folic acid; BSA, bovine serum albumin; ENs, ethoniosomes

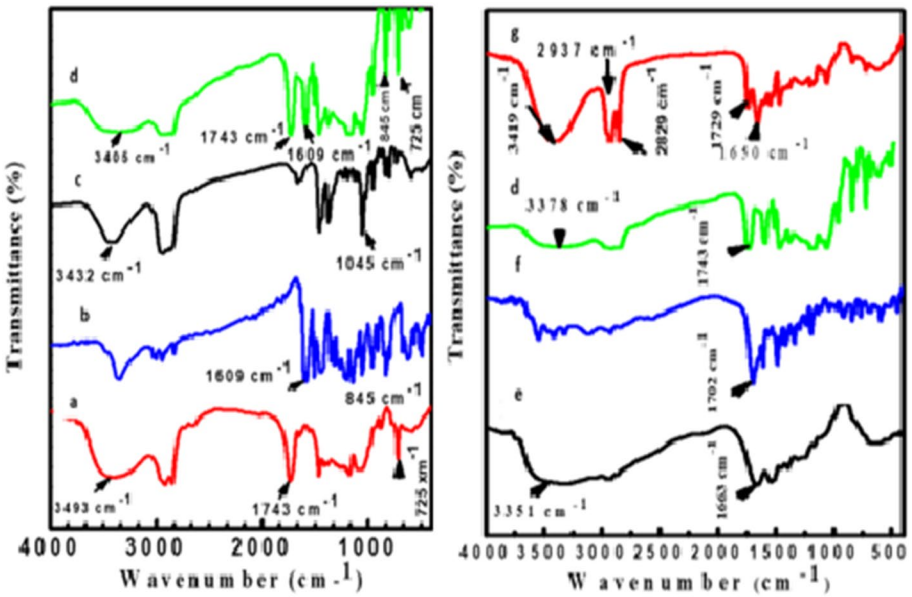

Fig. 7 FTIR spectra **a** Span 60, **b** PTS, **c** CHO, **d** PTS-loaded ENs, **e** BSA, **f** FA, and **g** FA-BSA-ENs of PTS
Abbreviations: PTS, pterostilbene; CHO, cholesterol; PTS-loaded ENs, pterostilbene -loaded ethoniosomal nanovesicles; BSA, albumin from bovine serum; FA, folic acid

During aliphatic CH stretching, asymmetric and symmetric were located at 2916 cm^{-1} and 2849 cm^{-1}, respectively. Meanwhile, the aliphatic –CH2– rocking was shown at 845 cm^{-1}. CHO showed characteristic peaks at 802 cm^{-1}, 1045 cm^{-1}, and 2900 cm-1 due to methylene rocking, C–O stretching, and C–H bond stretching. A broad peak appeared in the range of 3100– 3600 cm^{-1} associated with –OH stretching (Farmoudeh et al. 2020).

The main characteristic peaks of CHO, span 60, and PTS were displayed in the spectrum of PTS-loaded ENs. A strong peak found in the range 3000–3700 cm^{-1} may be attributed to a hydrogen bond interaction between the components of ENs (mostly CHO and span 60). The FTIR spectrum of BSA exhibited a band located at 1663 cm^{-1} that was attributed to the characteristic amide I band. The band located at 3351 cm^{-1} was attributed to primary amines. The band appeared at 2958.79 cm^{-1} was corresponded to C–H vibration (Nosrati et al. 2018).

The spectra of FA showed the carboxyl –C=O located at 1702 cm^{-1} (Zhang, et al. 2014), and the peak observed at 838 cm^{-1} was associated with the para-disubstituted benzene ring (Vikas,, et al. 2021). The spectrum of FA-BSA-ENs of PTS showed FA characteristic peaks, such as –C=O at 1702 cm^{-1}, and the characteristic peaks of BSA can be observed at 1663 cm^{-1} as well. Additionally, the band located at 3351 cm^{-1} could be attributed to primary amines. The band that appeared at 2958.79 cm^{-1} corresponded to C–H vibration in addition to the characteristic bands of PTS-loaded ENs detected. The obtained result ensured good physicochemical interaction between the drug and excipients.

Table 9 Effect of storage on the properties of optimized ethoniosomal formula

Parameter	PTS-loaded ENs		FA-BSA-ENs of PTS	
	Fresh	Stored	Fresh	Stored
EE (%)	93.19 ± 0.66	91.38 ± 0.22	93.32 ± 0.48	91.49 ± 0.51
Q_{24h} (%)	75.10 ± 1.90	71.34 ± 1.93	72.03 ± 1.41	70.19 ± 1.42

Each value represents mean ± SD ($n = 3$), optimized PTS-loaded ENs is F4, optimized FA-BSA-ENs of PTS (lung-targeted F4)

EE, entrapment efficiency; Q_{24h}, % drug released after 24 h; PTS-loaded ENs, pterostilbene-loaded ethoniosomal nanovesicles

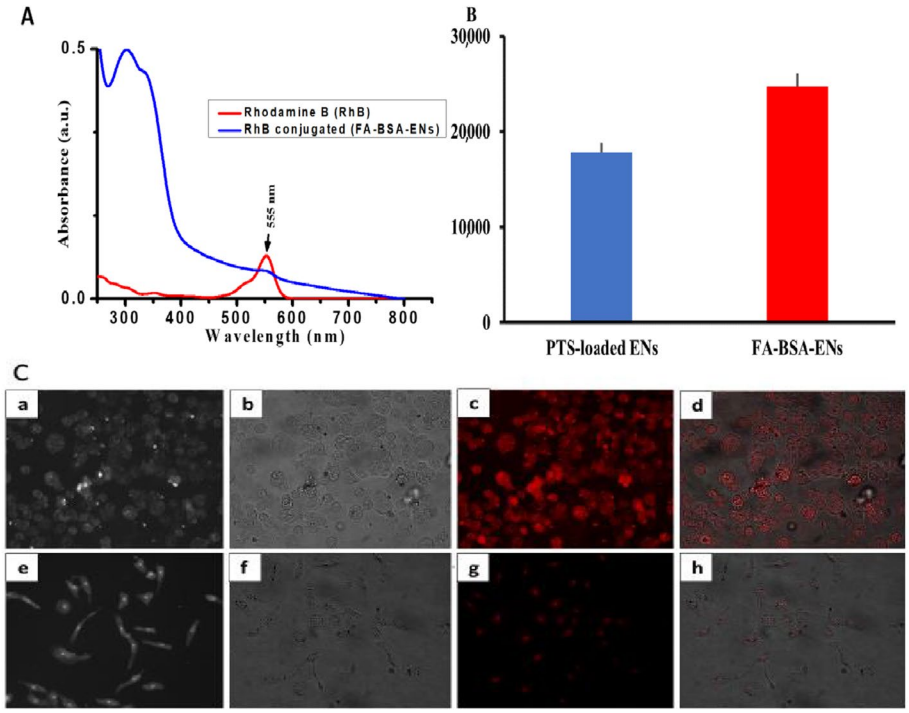

Fig. 8 UV visible of RhB conjugated to FA-BSA-ENs or PTS-loaded ENs **A**. Fluorescence image of FA-BSA-ENs-conjugated RhB. **B** Qualitative cell internalization assay using RhB-conjugated different nanoparticles using fluorescence microscopy. **C** Fluorescence images demonstrate cellular internalization of FA-BSA-ENs-conjugated RhB in A549 cells; **a** The grayscale image. **b** Transmission (white–black) image. **c** TRIC channel of RhB **d** merge between the transmission image and TRIC channel by using the Image j program. Fluorescence images demonstrate cellular internalization of PTS-loaded ENs-conjugated RhB in A549 cells; **e** The grayscale image. **f** Transmission (white–black) image. **g** the TRIC channel of RhB **h** merges between the transmission image and the TRIC channel by using the Image j program

The effect of storage on the stability of the optimized ethoniosomal formula.

The stability of the FA-BSA-ENs of PTS and PTS-loaded ENs was studied for three months at 4–8 ○C (Table 9). No change in the appearance of the FA-BSA-ENs of PTS and PTS-loaded ENs was detected during storage. Furthermore, stored FA-BSA-ENs and PTS-loaded ENs showed no significant change in the EE% and $Q_{24h\%}$ when compared with the fresh ethoniosomal formulations ($p > 0.05$). Moreover, the in vitro release profile of the ethoniosomal formula exhibited an insignificant difference after storage ($p > 0.05$). So these ethoniosomes can be an effective formulation with good stability and it is better to store them at 4–8 °C. These results agreed with Rehman et al. (Rehman et al. 2018).

Cellular uptake and targeting capacity

The targeting capacity of FA-BSA-ENs internalized inside A549 cells was measured by fluorescence microscopy. Rhodamine-labeled FA-BSA-ENs (Fig. 8A) were successfully localized inside the cytoplasm, as demonstrated by the intensity of fluorescence emission of red color located in the perinuclear region compared to PTS-loaded ENs (Fig. 8B, C). Fluorescence images demonstrate that FA-BSA-ENs conjugated to FA were readily accumulated in cellular compartments leading to increase drug capacity and efficiency. These results agreed with Zayed et al. (Mabrouk Zayed et al. 2022) who demonstrated that apigenin nanoparticles conjugated to FA were accumulated in cellular compartments leading to increase drug capacity and efficiency. Meanwhile, CTCF was estimated after 24 incubation for targeted FA-BSA-ENs and PTS-loaded ENs as 24643 and 17784, respectively. This indicates that the accumulation of nanoparticles in cancer cells depends also on their functionalization with ligand-targeted delivery (Hanafy et al. 2023).

Cytotoxicity study

MTT assay is a colorimetric technique that can be used to measure cellular metabolic activity based on the transformation of a yellow tetrazolium salt (3-(4, 5-dimethylthiazol-2-yl)-2,5-diphenyltetrazolium bromide or MTT) by metabolically active cells into purple formazan crystals. These crystals can be dissolved by using DMSO and then the color was measured at 540 nm.

In the present study, the MTT assay was utilized to evaluate the anti-tumor effects of serial concentrations (0.1, 1, 10, 100, and 1000 µg/ml) from PTS, PTS-loaded ENs, and FA-BSA-ENs of PTS in non-small lung cancer cell line using A549 cells. Based on cellular proliferation, A549 cells were significantly inhibited after 72 incubation with 1000 µg/ml (PTS, PTS-loaded ENs, and FA-BSA-ENs of PTS by $1.4 \pm 2.7\%$, $0.18 \pm 0.7\%$, and $0.15 \pm 1.7\%$ $P \leq 0.001$, respectively) (Fig. 9). The IC50 of FA-BSA-ENs of PTS ensures that the delivery system for PTS was more cytotoxic than PTS-loaded ENs on A549 cells (17.96 ± 0.65 µg/ml and 24.83 ± 0.88 µg/ml, respectively). Free PTS treatment demonstrated higher cytotoxicity compared with PTS-loaded ENs due to the slow release of ENs. These findings showed that targeted FA-BSA-ENs provide highly significant

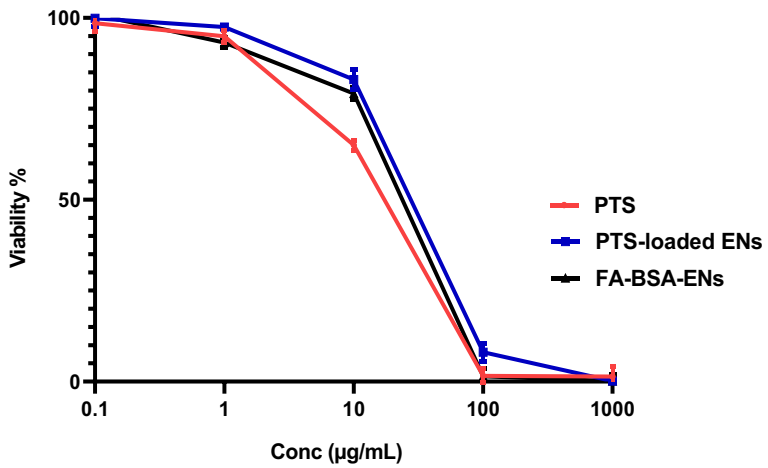

Fig. 9 In vitro cytotoxicity of free PTS, PTS-loaded ENs, and FA-BSA-ENs of PTS against A-549 lung cancer cell

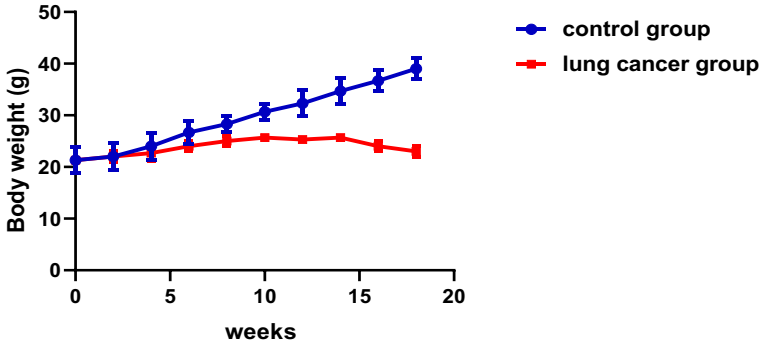

Fig. 10 The change in mice body weight during induction of lung cancer

cellular uptake because of the presence of FA as a target for FR compare to non-targeted PTS-loaded ENs.

The in vivo anti-tumor efficacy study

The lung cancer group (positive control) exhibited a significant loss of body weight during induction of lung cancer compared to the negative control ($P < 0.05$) (Fig. 10). The finding of this current study agreed with Xin et al. (Xin et al. 2017) who observed loss of body weight during hepatocellular carcinoma induction. These results were supported by histopathological analysis of the current study.

To observe the potential efficacy of targeted FA-BSA-ENs of PTS on the proliferation of lung cancer cells, compared to non-targeted PTS-loaded ENs, and free PTS, the histopathological investigation and immunohistochemistry profile were used.

Histopathological evaluation

The microscopic images of H&*E*-stained lung sections were used to evaluate the influence of oral administration of targeted FA-BSA-ENs of PTS, non-targeted PTS-loaded ENs, and free PTS on lung cancer and then were compared with positive control. The lung sections in normal mice showed normal alveoli were lined with a single epithelial cell layer.

However, lung parenchyma was mainly replaced by a large tumor mass in the lung cancer model (positive control) (Sivalingam et al. 2019).

Additionally, the size of tumor mass was significantly reduced in the treated groups in the following order: free PTS > non-targeted PTS-loaded ENs (140.126 ± 1.24, and 122.06 ± 3.64 μm, respectively) ($P < 0.001$).

FA-BSA-ENs produced a high potential effect on the invasiveness of lung cancer. There was no tumor mass observed. Meanwhile, mildly congested blood vessels and perivascular leukocytic cell infiltration were observed (Zou, et al. 2021) (Fig. 11).

Normal appearance of lung section was observed in control mice that were given targeted FA-BSA-ENs, non-targeted PTS-loaded ENs, and free PTS.

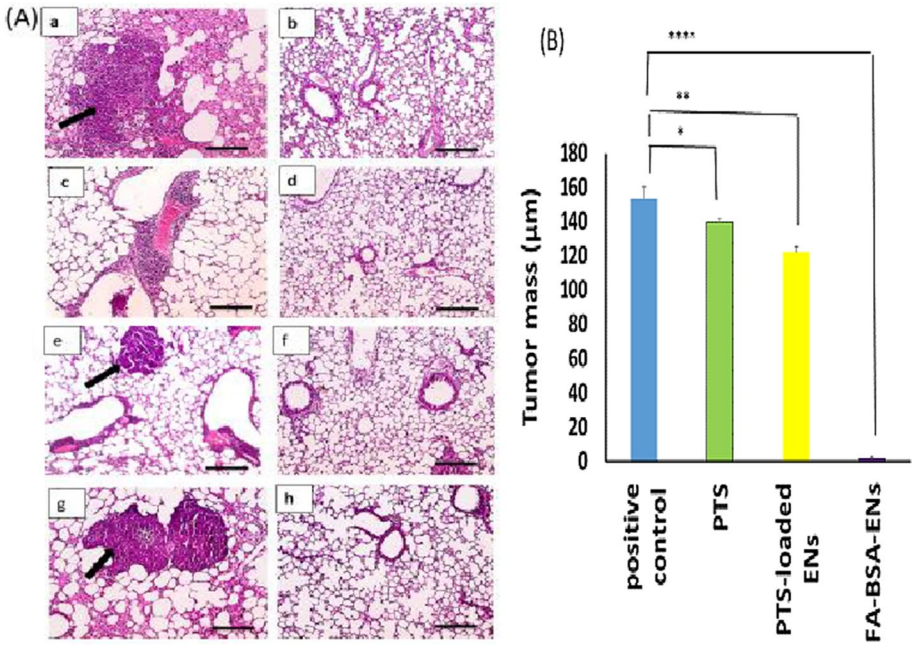

Fig. 11 **A** Microscopic images of H&E-stained lung sections: **a** lung cancer group (positive control group), **b** healthy normal mice without treatment (negative control group), **c** lung cancer group treated with FA-BSA-ENs of PTS, **d** control group treated with FA-BSA-ENs of PTS, (**e**) lung cancer group treated with PTS-loaded ENs, **f** control group treated with PTS-loaded ENs, **g** lung cancer group treated with free PTS, **h** control group treated with free PTS (X: 100 bar 100 µm). **B** Statistical analysis of the surface area of the tumor (µm) of treated groups vs. positive control group (****: p-value < 0.0001, **: p-value < 0.01, *: p-value < 0.05)

However, the lung sections from the lung cancer model showed severe inflammation, collapsed alveoli, alveolar emphysema, alveolar edema, and tumor focus (bronchogenic carcinoma).

The current finding suggested that oral administration of PTS promotes a strong protective effect against the proliferation of lung cancer cells improving the histopathological evidence of lung cancer and removing completely the lung nodules in a maximum dose of 100 mg/mL each day for 14 days. The result is fully in agreement with (Bracht et al. 2019) who reported that PTS is a better potential candidate for more effectively treating lung cancer.

With the targeting therapy, the results indicate that targeted FA-BSA-ENs of PTS obtained potential cytotoxicity for cancer cells. Therefore, it reduced tumor mass compared to non-targeted PTS-loaded ENs and free PTS.

Similar results were also found in folic acid-polyethylene glycol-cisplatin conjugates. In this case, a higher uptake was detected in lung cancer cells overexpressing folate receptors (He et al. 2015).

Immunohistochemistry analysis

Caspase-3 is an apoptotic indicator of cell cleavage and has an extensive role in apoptotic cell death. In the current study, the immunohistochemistry of cleaved caspase-3 was obtained by using formalin-fixed paraffin-embedded lung sections to investigate

the effect of targeted FA-BSA-ENs of PTS, non-targeted PTS-loaded ENs, and free PTS on the activation of the apoptotic pathway in bronchogenic carcinoma lung model. Immune-stained sections of the lung cancer group treated with targeted FA-BSA-ENs showed significantly strong positive brown expression of caspase-3 (44.7 ± 3.8, $P < 0.0001$) (Mabrouk Zayed, et al. 2022). However, this expression was gradually reduced significantly in the lung cancer group treated by using non-targeted PTS-loaded ENs (13.3 ± 3.6, $P < 0.001$) which appeared as a moderate positive brown expression. The lung cancer group treated with free PTS was observed (7.8 ± 2.5, $P < 0.01$) with mild positive brown expression. In contrast, the negative control (untreated group) obtained less expression of caspase level (4 ± 0.98).

Similarly, control groups that received orally targeted FA-BSA-ENs, non-targeted PTS-loaded ENs, and free PTS exhibited normal expression of caspase-3. Meanwhile, there is no expression of caspase-3 was shown in the lung cancer model (positive control). Since immunohistochemical reaction of caspase 3 stained sections observed very few brown appearances (Fig. 12).

The current data indicated that PTS promoted the induction of apoptosis by activating the caspase cascade and inducing changes in several cell cycle-regulating proteins, which is in agreement with the results of Tan et al. (Tan et al. 2019). Similarly, wen et al. reported that PTS could induce apoptotic activity in ovarian cancer cells. Based on our current study and the previous reports, PTS could effectively inhibit the cell viability of the lung cancer model by promoting apoptosis (Wen, et al. 2018).

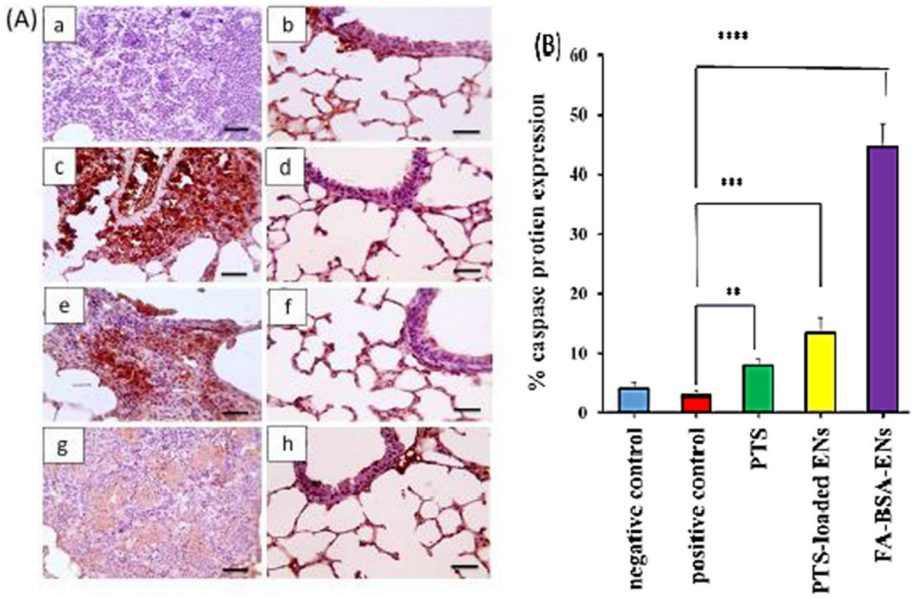

Fig. 12 **A** Immunohistochemistry analyzed caspase-3 in lung sections: **a** lung cancer group (positive control group), **b** healthy normal mice without treatment (negative control group), **c** lung cancer group treated with FA-BSA-ENs of PTS, **d** control group treated with FA-BSA-ENs of PTS, **e** lung cancer group treated with PTS-loaded ENs, **f** control group treated with PTS-loaded ENs, **g** lung cancer group treated with free PTS, **h** control group treated with free PTS (X: 400 bar 50 µm). **B** Statistical analysis of % caspase-3 expression of lung sections of treated groups vs. positive control group (****: *p*-value < 0.0001, ***: *p*-value < 0.001, **: *p*-value < 0.01)

Meanwhile, the result demonstrated that FA-BSA-ENs of PTS obtained much potential therapeutic and pharmacokinetic activity of PTS leading to an increase in the cellular uptake and improving the pharmacological activity of PTS, meaning that FA significantly increased the accumulation of PTS in the specific area of lung cancer cells. The result is in agreement with Martín-Sabroso et al. and Geersing et al. (Martín-Sabroso, et al. 2021; Geersing et al. 2019).

Histopathology evaluation of liver, kidney, and heart

Microscopic images of H&E-stained heart sections from the lung cancer model showed prominent interstitial mononuclear cell infiltration among ventricular and auricular muscle fibers compared to the control group (Abdel-Moneim et al. 2017). However, the normal appearance of heart sections was observed in control mice that received saline, targeted FA-BSA-ENs of PTS, non-targeted PTS-loaded ENs, and free PTS.

On the other hand, heart sections of the lung cancer group treated orally with targeted FA-BSA-ENs showed mild interstitial mononuclear cell infiltration distributed in between ventricular muscle fibers.

Meanwhile, heart sections from lung cancer treated orally with non-targeted PTS-loaded ENs and free PTS groups showed there was no interstitial leukocytic cell infiltration distributed in ventricular or auricular muscle fibers (Fig. 13).

Microscopic images of H&E stained showed a normal appearance of the liver section from the control group that received saline, targeted FA-BSA-ENs of PTS, non-targeted PTS-loaded ENs, and free PTS. However, the lung cancer model observed marked perivascular inflammation, fibrosis, and focal areas of coagulative necrosis

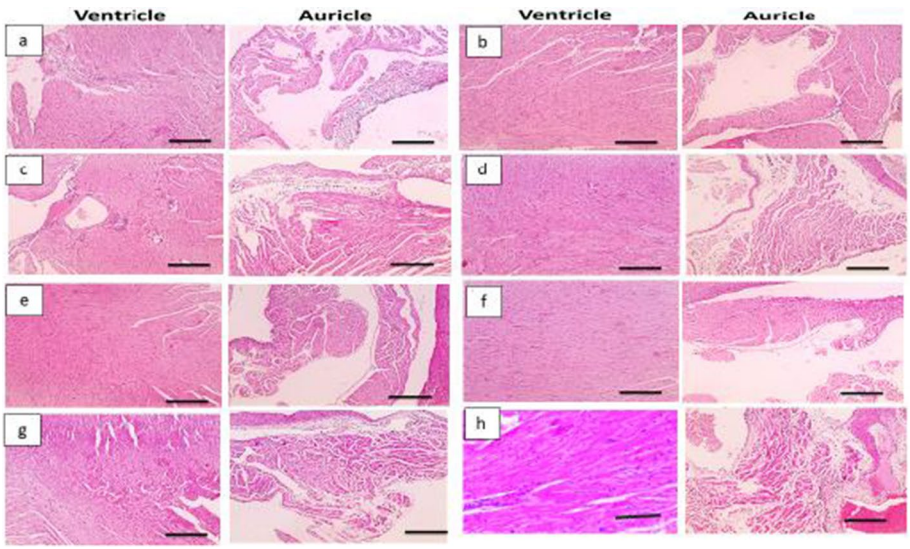

Fig. 13 Microscopic images of H&E-stained heart sections: **a** lung cancer group (positive control group), **b** healthy normal mice without treatment (negative control group), **c** lung cancer group treated with FA-BSA-ENs of PTS, **d** control group treated with FA-BSA-ENs of PTS, **e** lung cancer group treated with PTS-loaded ENs, **f** control group treated with PTS-loaded ENs, **g** lung cancer group treated with free PTS, **h** control group treated with free PTS (X: 100 bar 100 µm)

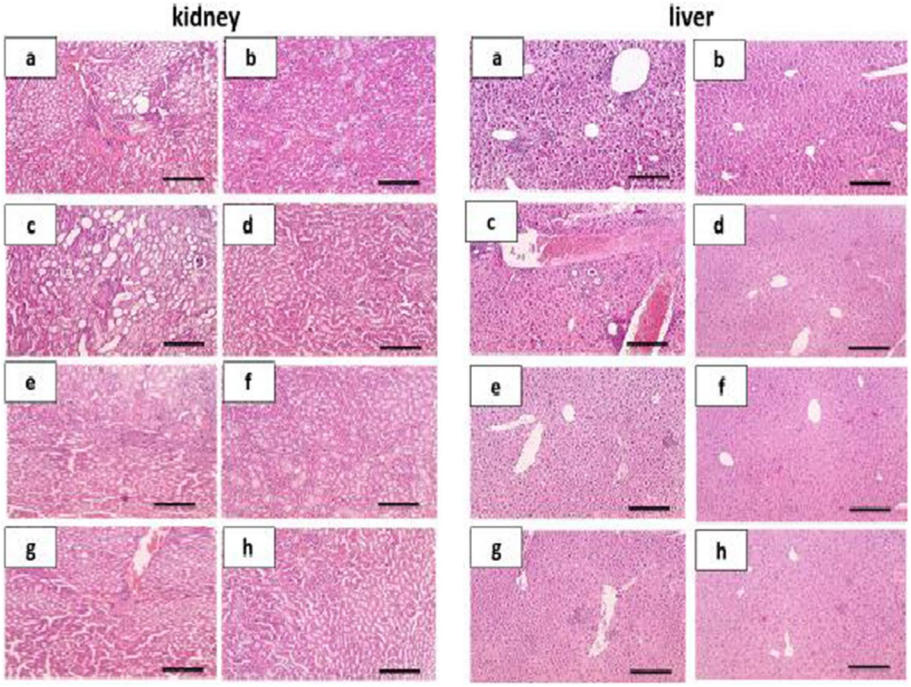

Fig. 14 Microscopic images of H&E stained kidney and liver sections: **a** lung cancer group (positive control group), **b** healthy normal mice without treatment (negative control group), **c** lung cancer group treated with FA-BSA-ENs of PTS, **d** control group treated with FA-BSA-ENs of PTS, **e** lung cancer group treated with PTS-loaded ENs, (**f**) control group treated with PTS-loaded ENs, **g** lung cancer group treated with free PTS, **h** control group treated with free PTS (X: 100 bar 100 µm)

in hepatocytes (Mansour et al. 2019). Nevertheless, the lung cancer group treated with FA-BSA-ENs of PTS showed similar pathological features from congested portal veins, portal inflammation, fibrosis, and coagulative necrosis in hepatocytes. This indicated extensively that FA-BSA-ENs of PTS were not absorbed by liver cells even if they were circulated through sinusoids. Such a result was confirmed in the lung cancer group treated with non-targeted PTS-loaded ENs that showed good histological architecture with only very mild inflammation. Meanwhile, the lung cancer group treated by using free PTS observed mildly congested blood vessels decreased inflammation, and few necrotic hepatocytes (Fig. 14). This means that PTS can reduce and improve inflammation induced by DENA in case loading it in carriers. However, the delivery of PTS from FA-BSA-ENs of PTS is mostly controlled by FA to be more specific delivery into a certain area.

In the renal section, the microscopic images of the lung cancer model showed congested blood vessels, perivascular mononuclear cell infiltration, and tubular dilation with loss of brush borders (Gani et al. 2019). Similarly, the FA-BSA-ENs group showed congested blood vessels with moderate perivascular mononuclear cell infiltration and tubular dilation with loss of brush borders with moderate perivascular mononuclear cell infiltration. The result confirmed that no absorbance of PTS from FA-BSA-ENs was done by kidney cells. To provide a clear understanding, non-targeted PTS-loaded ENs and free PTS were also used. The pathological evidence confirmed the presence of moderately congested blood vessels with mild perivascular

mononuclear cell infiltration in the group treated with free PTS. However, most improvements were seen in the group treated with non-targeted PTS-loaded ENs (Fig. 14).

The histopathological results of the heart, liver, and kidney indicated that the improvement of histo-architecture of organs was obtained in groups treated orally by using non-targeted PTS-loaded ENs > free PTS > targeted FA-BSA-ENs. The results demonstrated that folate receptors are overexpressed on the surface of many cancer cells, such as ovarian, lung, colon, and endometrial carcinoma, while their expression is limited in other cells. Thus, interesting tumor cells could bind to associated ligands in cancer therapies which is in full agreement with our obtained results (Chen et al. 2013).

This proved that FA conjugated to PTS-loaded ENs allowed a specific targeting to folate receptor overexpressing cancer cells and allowed targeted inhibition of lung cancer.

In the current study, the pathological profile scores of heart, liver, and kidney damages in the lung cancer model were calculated according to hanafy et al. (Hanafy and El-Kemary 2022). Histopathological examination was performed and mononuclear infiltrations, congested blood vessels, necrosis inflammation, and tubular dilatation with loss of brush borders were evaluated. The grading scale pathologic finding was as follows: 0 = no injury; 1 = slight injury; 2 = moderate injury; 3 = severe injury; and 4 = very severe injury (Fig. 15).

From the above data, it is obvious that FA-BSA-ethoniosomal formulation is a promising technique that could improve the effect of PTS for lung cancer treatment. These findings open the door to future use of ethoniosomes for different routes of administration, such as transdermal drug delivery system that could overcome the first pass effect. We recommend using FA-BSA-ethoniosomes of PTS as a targeted drug delivery system for different types of cancers, such as liver and breast cancer. In the future, we also suggest adding an edge activator to ethoniosomes to make synergism between ethanol and edge activator in order to improve the flexibility and permeability of ethoniosomes.

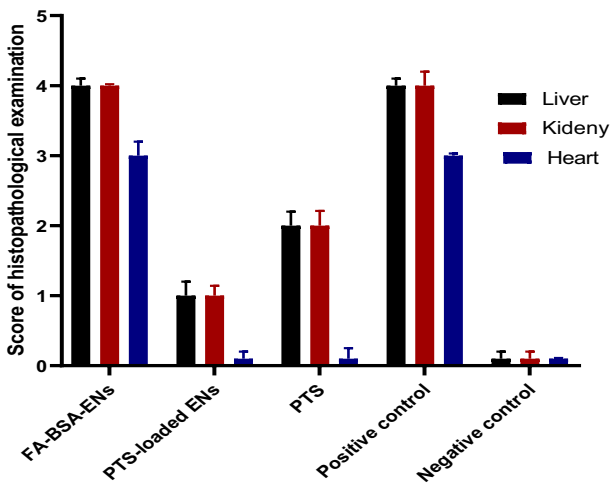

Fig. 15 Scores of histopathological examinations of the liver, kidney, and heart

Conclusion

In this work, we developed and evaluated a PTS-loaded ethoniosomal delivery system by Design-Expert® using formulation variables: the amount of span 60, the amount of ethanol, and the amount of CHO. The optimized ethoniosomal formulation (F4) was chosen based on maximizing both EE% and Q_{24h} according to the desirability criteria. FA conjugated to the optimized ethoniosomal formulation using BSA in order to target the folate receptor overexpressing cancer cells. The FA-BSA-ENs of PTS showed spherical morphology with a size of 144.05 ± 1.77 nm and a zeta potential of − 38.6 mV. The FA-BSA-ENs demonstrated high stability and deformability. The FA-BSA-ENs internalized into cancer cells via receptor-mediated endocytosis and allowed targeted inhibition of lung cancer. The histopathological examination of lung sections and caspase-3 immunoassay demonstrated that FA-BSA-ENs of PTS obtained much potential therapeutic and pharmacokinetic activity of PTS leading to an increase in the cellular uptake and improving the pharmacological activity of PTS. According to the results, FA-BSA-ethoniosomal vesicles can be a promising targeted drug delivery system for lung cancer treatment.

Supplementary Information

The online version contains supplementary material available at https://doi.org/10.1186/s12645-023-00197-4.

Additional file 1: Figure S1. The diagnostic graphs of EE% for PTS-loaded ENs (a) normal probability graph of residuals, (b) graph between residuals versus predicted values, (c) graph between residuals versus run number, and (d) graph between predicted versus actual values. **Figure S2.** The diagnostic graphs of Q_{24h} of PTS-loaded ENs (a) normal probability graph of residuals, (b) graph between residuals versus predicted values, (c) graph between residuals versus run number, and (d) graph between predicted versus actual values. **Figure S3.** The impact of the selected variables on the EE % of PTS-loaded ENs (a) amount of cholesterol, (b) amount of span, and (c) amount of ethanol. Abbreviations: PTS, pterostilbene; EE, entrapment efficiency. **Figure S4.** The impact of the selected variables on the Q_{24h} of PTS-loaded ENs (a) amount of cholesterol, (b) amount of span, and (c) amount of ethanol. Abbreviations: PTS, pterostilbene; Q_{24h}, %PTS released after 24 h.

Acknowledgements

Reham H. abdelbadea would like to thank professor Dr. Abdelaziz E. Abdelaziz and Eman A. Mazyed for their kind supervision, support, and their encouragement, and Nemany A.N. Hanafy for his great supervision and his ability to facilitate all my practical work and did not save any effort or time to support me in accomplishing this work.

Author contributions

NANH contributed to methodology, data curation, investigation, writing original draft, preparation, design the manuscript, format analysis, reviewing and editing original draft, and supervision. RHA was involved in methodology, data curation, investigation, format analysis, writing original draft. AEA contributed to investigation, manuscript designing, reviewing and editing original draft, and supervision. EAM performed supervision, review and editing, and investigation and designed the manuscript. All the authors have read and agreed to the published version of the manuscript. All the authors read and approved the final manuscript.

Funding

This research received no any funds.

Availability of data and materials

Data are available in a publicly accessible repository.

Declarations

Ethics approval and consent to participate

All experiments were conducted in accordance with US National Institutes of Health Guidelines for the Care and Use of Laboratory Animals and cell line experiments Guide for the Care and Use of Laboratory Animals after being approved by the relevant Ethical Committee and authorized by the Italian and German Ministry of Health. This study was also approved by the Research Ethics Committee of Kafrelsheikh University (KFS.Ph.001/21).

Consent for publication

All the authors have provided their agreement to publish the submitted manuscript.

Competing interests

The authors declare no competing interests.

Received: 22 January 2023 Accepted: 12 April 2023
Published online: 08 May 2023

References

Abdel-Hamid NM et al (2018) Expression of thioredoxin and glutaredoxin in experimental hepatocellular carcinoma-Relevance for prognostic and diagnostic evaluation. Pathophysiology 25(4):433–438
Abdel-Hamid NM et al (2022) Dual regulating of mitochondrial fusion and Timp-3 by leflunomide and diallyl disulfide combination suppresses diethylnitrosamine-induced hepatocellular tumorigenesis in rats. Life Sci 294:120369
Abdel-Moneim A et al (2017) The preventive effects of avocado fruit and seed extracts on cardio-nephrotoxicity induced by diethylnitrosamine/2-acetylaminoflurine in wistar rats. Basic Sci Med 6(1):4–13
Ahad A et al (2013) Enhanced transdermal delivery of an anti-hypertensive agent via nanoethosomes: statistical optimization, characterization and pharmacokinetic assessment. Int J Pharm 443(1–2):26–38
Allam RM et al (2018) Fingolimod interrupts the cross talk between estrogen metabolism and sphingolipid metabolism within prostate cancer cells. Toxicol Lett 291:77–85
Anbarasan B et al (2013) Optimization of the formulation and in-vitro evaluation of capecitabine niosomes for the treatment of colon cancer. Int J Pharm Sci Res 4(4):1504
Araújo J et al (2010) Optimization and physicochemical characterization of a triamcinolone acetonide-loaded NLC for ocular antiangiogenic applications. Int J Pharm 393(1–2):167–175
Arzani G et al (2015) Niosomal carriers enhance oral bioavailability of carvedilol: effects of bile salt-enriched vesicles and carrier surface charge. Int J Nanomedicine 10:4797–4813
Badria FA et al (2020a) Development of provesicular nanodelivery system of curcumin as a safe and effective antiviral agent: statistical optimization, in vitro characterization, and antiviral effectiveness. Molecules. https://doi.org/10.3390/molecules25235668
Badria FA et al (2020b) Formulation of sodium valproate nanospanlastics as a promising approach for drug repurposing in the treatment of androgenic alopecia. Pharmaceutics. https://doi.org/10.3390/pharmaceutics12090866
Bansal S et al (2013) Design and development of cefdinir niosomes for oral delivery. J Pharm Bioallied Sci 5(4):318–325
Bernsdorff C et al (1997) Effect of hydrostatic pressure on water penetration and rotational dynamics in phospholipid-cholesterol bilayers. Biophys J 72(3):1264–1277
Bracht JWP et al (2019) Osimertinib and pterostilbene in EGFR-mutation-positive non-small cell lung cancer (NSCLC). Int J Biol Sci 15(12):2607–2614
Chen C et al (2013) Structural basis for molecular recognition of folic acid by folate receptors. Nature 500(7463):486–489
Chen RJ et al (2018) Apoptotic and nonapoptotic activities of pterostilbene against cancer. Int J Mol Sci. https://doi.org/10.3390/ijms19010287
Eid RK, Essa EA, El Maghraby GM (2019) Essential oils in niosomes for enhanced transdermal delivery of felodipine. Pharm Dev Technol 24(2):157–165
El Maghraby GM, Williams AC, Barry BW (2004) Interactions of surfactants (edge activators) and skin penetration enhancers with liposomes. Int J Pharm 276(1–2):143–161
El Maghraby GM, Ahmed AA, Osman MA (2014) Skin delivery of nisoldipine from niosome proconcentrate. J Appl Pharm Sci 4:112–117
El Maghraby GM, Ahmed AA, Osman MA (2015) Penetration enhancers in proniosomes as a new strategy for enhanced transdermal drug delivery. Saudi Pharm J 23(1):67–74
El-Samaligy MS, Afifi NN, Mahmoud EA (2006) Increasing bioavailability of silymarin using a buccal liposomal delivery system: preparation and experimental design investigation. Int J Pharm 308(1–2):140–148
Essa ML et al (2022) Dual targeting nanoparticles based on hyaluronic and folic acids as a promising delivery system of the encapsulated 4-Methylumbelliferone (4-MU) against invasiveness of lung cancer in vivo and in vitro. Int J Biol Macromol 206:467–480
Estrela JM et al (2013) Pterostilbene: biomedical applications. Crit Rev Clin Lab Sci 50(3):65–78
Farmoudeh A et al (2020) Methylene blue-loaded niosome: preparation, physicochemical characterization, and in vivo wound healing assessment. Drug Deliv Transl Res 10(5):1428–1441
Gaafar PM et al (2014) Preparation, characterization and evaluation of novel elastic nano-sized niosomes (ethoniosomes) for ocular delivery of prednisolone. J Liposome Res 24(3):204–215
Gani SA et al (2019) Effect of protocatechuic acid-layered double hydroxide nanoparticles on diethylnitrosamine/phenobarbital-induced hepatocellular carcinoma in mice. PLoS ONE 14(5):e0217009
Geersing A et al (2019) Folic acid conjugates of a bleomycin mimic for selective targeting of folate receptor positive cancer cells. Bioorg Med Chem Lett 29(15):1922–1927
Grossi F et al (2010) Future scenarios for the treatment of advanced non-small cell lung cancer: focus on taxane-containing regimens. Oncologist 15(10):1102–1112
Hanafy NA, El-Kemary MA (2022) Silymarin/curcumin loaded albumin nanoparticles coated by chitosan as muco-inhalable delivery system observing anti-inflammatory and anti COVID-19 characterizations in oleic acid triggered lung injury and in vitro COVID-19 experiment. Int J Biol Macromol 198:101–110
Hanafy NAN et al (2017) Hybrid polymeric-protein nano-carriers (HPPNC) for targeted delivery of TGFbeta inhibitors to hepatocellular carcinoma cells. J Mater Sci Mater Med 28(8):120
Hanafy NAN, Leporatti S, El-Kemary MA (2021) Extraction of chlorophyll and carotenoids loaded into chitosan as potential targeted therapy and bio imaging agents for breast carcinoma. Int J Biol Macromol 182:1150–1160
Hanafy NA et al (2023) Simultaneous administration of bevacizumab with bee-pollen extract-loaded hybrid protein hydrogel NPs is a promising targeted strategy against cancer cells. Int J Mol Sci 24(4):3548
He Z et al (2015) Co-delivery of cisplatin and paclitaxel by folic acid conjugated amphiphilic PEG-PLGA copolymer nanoparticles for the treatment of non-small lung cancer. Oncotarget 6(39):42150–42168

Inamura K (2017) Lung cancer: understanding its molecular pathology and the 2015 WHO Classification. Front Oncol 7:193
Kirby C, Clarke J, Gregoriadis G (1980) Effect of the cholesterol content of small unilamellar liposomes on their stability in vivo and in vitro. Biochem J 186(2):591–598
Larsson J (2009) Methods for measurement of solubility and dissolution rate of sparingly soluble drugs
Lee PS et al (2018) Chemoprevention by resveratrol and pterostilbene: targeting on epigenetic regulation. BioFactors 44(1):26–35
Leonyza A, Surini S (2019) Optimization of sodium deoxycholate-based transfersomes for percutaneous delivery of peptides and proteins. Int J Appl Pharm 11(5):329–332
Li H et al (2015) Folate-bovine serum albumin functionalized polymeric micelles loaded with superparamagnetic iron oxide nanoparticles for tumor targeting and magnetic resonance imaging. Acta Biomater 15:117–126
Liu Y et al (2020) Recent advances in synthesis, bioactivity, and pharmacokinetics of pterostilbene, an important analog of resveratrol. Molecules. https://doi.org/10.3390/molecules25215166
Liu Q et al (2021) Fabrication, characterization, physicochemical stability and simulated gastrointestinal digestion of pterostilbene loaded zein-sodium caseinate-fucoidan nanoparticles using pH-driven method. Food Hydrocoll 119:106851
Mabrouk Zayed MM et al (2022) The effect of encapsulated apigenin nanoparticles on HePG-2 cells through regulation of P53. Pharmaceutics 14(6):1160
Maestrelli F et al (2005) Preparation and characterization of liposomes encapsulating ketoprofen–cyclodextrin complexes for transdermal drug delivery. Int J Pharm 298(1):55–67
Mansour DF et al (2019) The carcinogenic agent diethylnitrosamine induces early oxidative stress, inflammation and proliferation in rat liver, stomach and colon: protective effect of ginger extract. Asian Pac J Cancer Prev 20(8):2551–2561
Mansouri M et al (2021) Streptomycin sulfate–loaded niosomes enables increased antimicrobial and anti-biofilm activities. Front Bioeng Biotechnol 9:745099
Martín-Sabroso C et al (2021) Active targeted nanoformulations via folate receptors: state of the art and future perspectives. Pharmaceutics. https://doi.org/10.3390/pharmaceutics14010014
Mavaddati MA, Moztarzadeh F, Baghbani F (2015) Effect of formulation and processing variables on dexamethasone entrapment and release of niosomes. J Cluster Sci 26:2065–2078
Mazyed EA, Abdelaziz AE (2020) Fabrication of transgelosomes for enhancing the ocular delivery of acetazolamide statistical optimization, in vitro characterization, and in vivo study. Pharmaceutics. https://doi.org/10.3390/pharmaceutics12050465
Mazyed EA et al (2021) Formulation and optimization of nanospanlastics for improving the bioavailability of green tea epigallocatechin gallate. Pharmaceuticals (basel). https://doi.org/10.3390/ph14010068
Mazyed EA et al (2022) Development of cyclodextrin-functionalized transethoniosomes of 6-gingerol: statistical optimization, in vitro characterization and assessment of cytotoxic and anti-inflammatory effects. Pharmaceutics 14(6):1170
Mehanna MM, Motawaa AM, Samaha MW (2015) Nanovesicular carrier-mediated transdermal delivery of tadalafil: i-formulation and physicsochemical characterization. Drug Dev Ind Pharm 41(5):714–721
Moghassemi S, Hadjizadeh A (2014) Nano-niosomes as nanoscale drug delivery systems: an illustrated review. J Control Release 185:22–36
Mokhtar M et al (2008) Effect of some formulation parameters on flurbiprofen encapsulation and release rates of niosomes prepared from proniosomes. Int J Pharm 361(1–2):104–111
Nasr M (2010) In vitro and in vivo evaluation of proniosomes containing celecoxib for oral administration. AAPS PharmSciTech 11(1):85–89
Nosrati H et al (2018) Folic acid conjugated bovine serum albumin: an efficient smart and tumor targeted biomacromolecule for inhibition folate receptor positive cancer cells. Int J Biol Macromol 117:1125–1132
Ola H, Yahiya SA, El-Gazayerly ON (2010) Effect of formulation design and freeze-drying on properties of fluconazole multilamellar liposomes. Saudi Pharm J 18(4):217–224
Pathan IB et al (2018) Curcumin loaded ethosomes for transdermal application: formulation, optimization, in-vitro and in-vivo study. J Drug Delivery Sci Technol 44:49–57
Peram MR et al (2019) Factorial design based curcumin ethosomal nanocarriers for the skin cancer delivery: in vitro evaluation. J Liposome Res 29(3):291–311
Rehman M et al (2018) Development and in vitro characterization of niosomal formulations of immunosuppressant model drug. Pak J Pharm Sci 31(6):2623–2628
Rezaie Amale F et al (2021) Gold nanoparticles loaded into Niosomes: a novel approach for enhanced antitumor activity against human ovarian cancer. Adv Powder Technol 32(12):4711–4722
Salem HF et al (2020) Mitigation of rheumatic arthritis in a rat model via transdermal delivery of dapoxetine HCl amalgamated as a nanoplatform: in vitro and in vivo assessment. Int J Nanomed 15:1517–1535
Salem HF et al (2021) Fabrication and appraisal of simvastatin via tailored niosomal nanovesicles for transdermal delivery enhancement: in vitro and in vivo assessment. Pharmaceutics. https://doi.org/10.3390/pharmaceutics13020138
Sezgin-Bayindir Z et al (2013) Niosomes encapsulating paclitaxel for oral bioavailability enhancement: preparation, characterization, pharmacokinetics and biodistribution. J Microencapsul 30(8):796–804
Shah H et al (2019) Proniosomal gel for transdermal delivery of lornoxicam: optimization using factorial design and in vivo evaluation in rats. Daru 27(1):59–70
Sivalingam K et al (2019) Neferine suppresses diethylnitrosamine-induced lung carcinogenesis in Wistar rats. Food Chem Toxicol 123:385–398
Skehan P et al (1990) New colorimetric cytotoxicity assay for anticancer-drug screening. J Natl Cancer Inst 82(13):1107–1112
Srinivas S et al (2010) Preparation and evaluation of niosomes containing aceclofenac. Dig J Nanomater Bios 5(1):249–254
Summerlin N et al (2015) Resveratrol nanoformulations: challenges and opportunities. Int J Pharm 479(2):282–290

Sun L et al (2014) Folic acid-functionalized up-conversion nanoparticles: toxicity studies in vivo and in vitro and targeted imaging applications. Nanoscale 6(15):8878–8883
Tan KT et al (2019) Pterostilbene inhibits lung squamous cell carcinoma growth in vitro and in vivo by inducing S phase arrest and apoptosis. Oncol Lett 18(2):1631–1640
Thakur C (2019) An overview, current challenges of drug resistance, and targeting metastasis associated with lung cancer. Elsevier, Amsterdam, pp 21–38
Touitou E et al (2000) Ethosomes—novel vesicular carriers for enhanced delivery: characterization and skin penetration properties. J Control Release 65(3):403–418
Turk CT et al (2014) Formulation and optimization of nonionic surfactants emulsified nimesulide-loaded PLGA-based nanoparticles by design of experiments. AAPS PharmSciTech 15(1):161–176
Tzeng WS et al (2021) Pterostilbene nanoparticles downregulate hypoxia-inducible factors in hepatoma cells under hypoxic conditions. Int J Nanomedicine 16:867–879
Vikas et al. (2021) Bioadhesive chitosan nanoparticles: Dual targeting and pharmacokinetic aspects for advanced lung cancer treatment. Carbohydr Polym. 274:118617.
Wen W et al (2018) Pterostilbene suppresses ovarian cancer growth via induction of apoptosis and blockade of cell cycle progression involving inhibition of the STAT3 pathway. Int J Mol Sci. https://doi.org/10.3390/ijms19071983
Xin B et al (2017) Combined use of alcohol in conventional chemical-induced mouse liver cancer model improves the simulation of clinical characteristics of human hepatocellular carcinoma. Oncol Lett 14(4):4722–4728
Zappa C, Mousa SA (2016) Non-small cell lung cancer: current treatment and future advances. Transl Lung Cancer Res 5(3):288–300
Zhang N et al (2014) Preparation, characterization, and in vitro targeted delivery of folate-conjugated 2-methoxyestradiol-loaded bovine serum albumin nanoparticles. J Nanoparticle Res. https://doi.org/10.1007/s11051-014-2390-6
Zhang Y et al (2014) Nanoemulsion for solubilization, stabilization, and in vitro release of pterostilbene for oral delivery. AAPS PharmSciTech 15(4):1000–1008
Zou Y et al (2021) Pterostilbene nanoparticles with small particle size show excellent anti-breast cancer activityin vitroandin vivo. Nanotechnology. https://doi.org/10.1088/1361-6528/abfdec

Publisher's Note